Characterizing the marine iodine cycle and its relationship to ocean deoxygenation in an Earth System model

Keyi Cheng[1], Andy Ridgwell[2], Dalton S. Hardisty[1]

[1]Department of Earth and Environmental Sciences, Michigan State University, East Lansing, 48823, USA

[2]Department of Earth and Planetary Sciences, University of California Riverside, Riverside, 92521, USA

Correspondence to: Keyi Cheng (chengkey@msu.edu)

Abstract. Iodine abundance in marine carbonates (measured as an elemental ratio with calcium – I:CaI/Ca) is of broad interest as a proxy for local/regional ocean redox. This connection arises because the speciation of iodine in seawater – in terms of the balance between iodate (IO_3^-) and iodide (I^-) – is sensitive to the prevalence of oxic vs. anoxic conditions. However, although I:CaI/Ca ratios are being increasingly commonly being measured in ancient carbonate samples, a fully quantitative interpretation of this proxy is hindered by the scarcity ofrequires the availability of a mechanistic and quantitative interpretative framework for the marine iodine cycle and that can account forits sensitivity to the extent and intensity of ocean deoxygenation in the past. Here we present and evaluate a representation of marine iodine cycling embedded in an Earth system model ('cGENIE') against both modern and paleo observations. In this framework, we account for IO_3^- uptake and reduction release of I^- through the biological pumpby primary producers, the occurrence ofreduction of ambient IO_3^- reductionto I^- in the water column, plus the re-oxidation of I^- to IO_3^-. We develop and test a variety of different plausible mechanistic mechanisms for iodine reduction and oxidation transformation relationships between IO_3^- and $I^-$and contrast model projections against an updated compilation of observed dissolved IO_3^- and I^- concentrations in the present-day ocean. In By optimizing the parameters controlling previously proposed mechanisms behind involved in marine iodine cycling, we find that we can obtain broad matches to observed iodine speciation gradients in zonal surface distribution, depth profiles, and oxygen deficient zones (ODZs). We However, we also identify alternative, equally well performing mechanisms which assume a more explicit mechanistic link between iodine transformation and environment – an. This mechanistic ambiguity that highlights the need for more process-based studies on modern marine iodine cycling. Finally, to help distinguish between competing representations of the marine iodine cycle and, because our ultimate motivation is to further our ability to reconstruct ocean oxygenation in the geological past, we conducted 'plausibility tests' of our various different model schemes against available I:CaI/Ca measurements made on Cretaceous carbonates – a time of substantially depleted ocean oxygen availability compared to modern and hence a strong test of our model. Overall, the simultaneous broad match we can achieve between modelled iodine speciation and modern observations, and between forward-proxy modelled I:CaI/Ca and geological elemental ratios, supports the application of our Earth system modelling in simulating the marine iodine cycle to help interpret and constrain the redox evolution of past oceans.

Formatted: Superscript

1. Introduction

Dissolved Iodine (I) in seawater is redox sensitive and as such, is a potential invaluable delineator of past ocean deoxygenation. This arises directly from: (1) observations that the oxidized form of iodine (iodate, IO_3^-) is reduced to iodide (I^-) under low oxygen conditions, and (2) that IO_3^- in seawater is incorporated into carbonate lattice during precipitation in proportion to its seawater abundance (whilst I^- is not) (Lu et al., 2010; Podder et al., 2017; Kerisit et al., 2018; Zhang et al., 2013; Hashim et al., 2022). ~~Hence~~As a result, past ocean IO_3^- concentrations can be recorded in coeval carbonates as ~~I:Ca~~I/Ca ratios, with the potential ~~of~~ for carbonate ~~I:Ca~~I/Ca to reflect the redox variation of the ancient seawater (Lu et al., 2010). Indeed, the ~~I:Ca~~I/Ca ratio in marine carbonates is already ~~widely~~ being applied widely as a paleoredox proxy, with studies employing it to explore ~~the~~ variations in the dissolved oxygen ([O_2]) concentration of seawater ~~variation~~ throughout much of Earth history, from the Archean and through the Cenozoic (Lu et al., 2010; Hardisty et al., 2014; Zhou et al., 2015; Lu et al., 2016; Edwards et al., 2018; Lu et al., 2018; Bowman et al., 2020; Pohl et al., 2021; Wei et al., 2021; Ding et al., 2022; Shang et al., 2019; Liu et al., 2020; Fang et al., 2022; Uahengo et al., 2020; Yu et al., 2022; Tang et al., 2023). ~~The~~ However, realizing the full potential for ~~I:Ca~~I/Ca to ~~generate~~ provide critical insights into how the oxygenation of the ocean has evolve through time, as well as the causes and biological/ecological consequences of this, requires that we have an adequate understanding, not only of carbonate IO_3^- incorporation, but of the dynamics of the marine iodine cycle in general.

~~Progress~~Considerable progress has been made over the past few decades towards the goal of understanding the marine iodine cycle ~~in the past decades~~. Iodine has a relatively long residence time in the ocean (~300 kyr; Broecker and Peng, 1983)~~,~~ ~~making~~ leading to its concentration ~~among~~ being relatively constant throughout the global ocean ~~relatively constant~~(at around 500 nM) (Elderfield and Truesdale, 1980; Truesdale et al., 2000; Chance et al., 2014). ~~Although~~ However, although the total concentration of dissolved iodine is relatively invariant, the two most abundant species of dissolved iodine in the ocean, IO_3^- and ~~iodide~~ I^-, vary relative to each other depending on the environment. Today, IO_3^- is generally the dominant iodine species in oxygenated regions of the ocean, where it ~~representing~~ represents total iodine nearly quantitatively below the euphotic zone. Within the euphotic zone, the concentration of I^- ~~occurs and~~ generally increases in association with release during phytoplankton growth and senescence (Hepach et al., 2020). ~~Iodide is also more abundant in oxygen deficient zones (ODZ) — often, but not always quantitatively so (Truesdale et al., 2000; Rue et al., 1997; Cutter et al., 2018; Moriyasu et al., 2020; Farrenkopf and Luther, 2002; Wong and Brewer, 1977; Truesdale et al., 2013; Rapp et al., 2020, 2019). Respectively, w~~Within ~~the ~~ODZs, IO_3^- is reduced to I^- ~~—~~but not always quantitatively so~~and hence is present only at relatively~~has low concentrations while I^- is abundant (Truesdale et al., 2000; Rue et al., 1997; Cutter et al., 2018; Moriyasu et al., 2020; Farrenkopf and Luther, 2002; Wong and Brewer, 1977; Truesdale et al., 2013; Rapp et al., 2020, 2019)~~(Rue et al., 1997; Farrenkopf et al., 1997; Moriyasu et al., 2020; Rapp et al., 2019, 2020)~~.

Although IO_3^- ~~is~~ generally depleted in low-[O_2] settings, the ~~causal~~ spatial relationship between seawater [O_2] and [IO_3^-] is not simple and is not currently ~~not~~ well understood. Recently published observations from ~~global oxygen deficient zones (~~ODZs~~)~~ in the ocean reveals that the relationship between dissolved [O_2] and [IO_3^-] is not linear, but instead it is possible that there is a certain [O_2] or related redox threshold associated with triggering IO_3^- reduction (Cutter et al., 2018; Moriyasu et al., 2020; Farrenkopf and Luther, 2002; Rue et al., 1997; Chapman, 1983).

72 Dissimilatory IO_3^- reducing bacteria, as well as abiotic reduction with sulfide and dissolved Fe, have been identified
73 within ODZs (Farrenkopf et al., 1997; Councell et al., 1997; Jiang et al., 2023). In addition, slow oxidation-reduction
74 kinetics (Tsunogai, 1971; Hardisty et al., 2020; Schnur et al., 2024) imply the likelihood that *in situ* iodine signals
75 could be integrated across large-scale physical oceanography processes – including ocean currents and mixing
76 between water masses (Hardisty et al., 2021), and meaning that iodine ~~species~~ speciation reflect~~s~~ ~~regional~~ ~~local~~regional
77 rather than strictly ~~local~~ in-situ redox conditions (Lu et al., 2020b). Non-redox related processes, such as
78 phytoplankton-mediated IO_3^- reduction and organic matter remineralization also exert~~s~~ controls on iodine speciation
79 in the water column (Fig. 1; Elderfield and Truesdale, 1980; Wong et al., 1985; Luther and Campbell, 1991; Hepach
80 et al., 2020). Therefore, it is difficult to infer water column redox simply based on iodine speciation without
81 considering these interacting physical and biological effects.

82

83

84

3
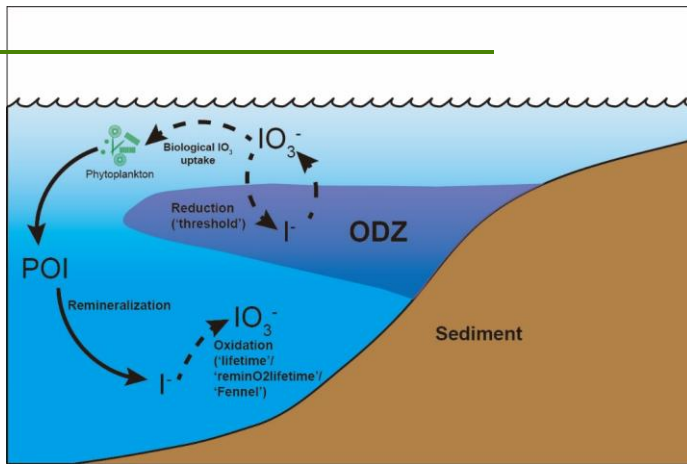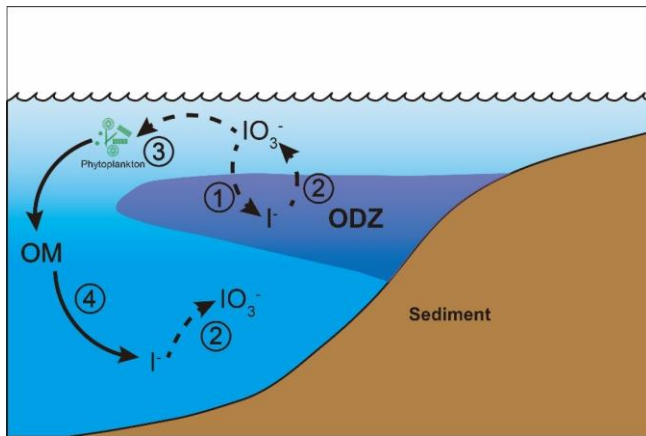
Figure 1: The iodine cycle in marine oxygen deficient zones (ODZ) in cGENIE including (1) IO_3^- reduction to I^-, (2) re-oxidation of I^- to IO_3^-, (3) photosynthetic IO_3^- update by phytoplankton, and (4) I^- releasement from organic matter (OM) through remineralization. The detailed oxidation-reduction options ('threshold' and 'lifetime'/ 'reminO2lifetime''reminO2lifetime'/ ''Fennel') are described in Section 2.2 and Table 1. Dashed arrows indicate variable processes during ensemble simulations. Note that the POI export is controlled by temperature (TDEP).

Apart Aside from the uncertainties associateds with IO_3^- reduction, it is notable that the oxidants responsible for IO_3^- formation during the I^- re-oxidation I^- are currently unknown, only that it is unlikely to be free O_2, which is not thermodynamically favorable to oxidize iodidne (Luther et al., 1995). A recent thermodynamic review indicates that the reactive oxygen species (ROS) such as hydrogen peroxide and OH radicals can fully oxidize I^- to IO_3^-. Iodide oxidation to IO_3^- is a 6-electron transfer and other ROS, such as superoxide, are only thermodynamically favorable to catalyze partial oxidation to intermediates (Luther, 2023). These ROS species have heterogenous distributions and ambient ocean concentrations that are typically relatively low compared to iodine, supporting the likelihood of temporally or spatially isolated high I^- oxidation rates despite of overall extremely slow rates (Schnur et al., 2024). Additional support for spatially or temporally heterogenous I^- oxidation rates comes from recent experimental observations of IO_3^- production from I^- in nitrifying cultures (Hughes et al., 2021). Nitrification (oxidation of NH_4^+ to NO_2^- (and NO_3^-)) rates vary globally, with the highest values occurring in ODZs and the dissolved deep chlorophyl maximum (summarized in Table 2 of Hughes et al., 2021). Regardless, nitrification or other specific mechanisms have yet to be linked directly to I^- oxidation under normal marine conditions, leaving open the question of rates and locations of I^- oxidation.

Despite a growing understanding of I:CaI/Ca variations through geologic time, it remains challenging to determine the mechanisms drivingresponsible for controlling the spatiotemporal patterns of marine $[IO_3^-]$ and the degree thathow these are linked to seawater oxygen and there have only been a few attempts to date to model the marine iodine cycle. Given the prevailing uncertainty in the mechanisms governing the marine iodine cycle mentioned above, and in conjunction with I:CaI/Ca being a relatively new proxy, it is perhaps not surprising that few attempts have been made to model the marine iodine cycle. In a recent publication, a model was developed to simulate modern ocean surface I^- distributions, with the aim of being able to improve tropospheric ozone models (Wadley et al., 2020). This particular model was based around a relatively high horizontal ocean resolution (1° grid size) with a 3-layer vertical upper water column. Iodine biogeochemical cycling was coupled with the nitrogen cycle, with the surface I^- distribution sensitive to biological and hydrological factors including primary productivity, I:C ratio, oxidation, mixed layer depth, advection, and freshwater flux. Because the Wadley et al., (2020) model was specifically focused on near-surface processes within the upper 500 m, it did not consider processes occurring within ODZs and hence is not directly applicable to questions concerning the controls on I:CaI/Ca ratios. In contrast, a second model-based study deliberately targeted paleoceanographic questions and incorporated an iodine cycle including redox-controlled biogeochemical reactions into the 'cGENIE' Earth system model (Lu et al., 2018). The advantage for paleo studies afforded by this particular approach is that the cGENIE model can take into account different continental configurations, non-modern atmospheric composition (pO$_2$, pCO$_2$), and other boundary conditions that may have

123 differed on ancient Earth relative to today (Ridgwell et al., 2007; Reinhard et al., 2016; Boscolo-Galazzo et al., 2021;
124 Remmelzwaal et al., 2019; Pohl et al., 2022; Reinhard and Planavsky, 2022).
125 ~~Despite a growing understanding of I:Ca~~I/Ca ~~variations through geologic time, it remains challenging to~~
126 ~~determine mechanisms driving spatiotemporal marine [IO₃⁻] and the degree that these are linked to seawater oxygen.~~
127 ~~Hence, the proxy is qualitative or semi-quantitative.~~ Here, we calibrate the iodine cycle within the cGENIE Earth
128 System model to provide a mechanistic framework for interpreting ancient ~~I:Ca~~I/Ca variations. In this study, we build
129 on the work of Lu et al., (2018) and further develop and test a series of new potential parameterizations for water
130 column iodine oxidation and~~,~~ reduction~~, cellular uptake, and release during remineralization~~ (in addition to reduction
131 and transport associated with the biological pump). We also developed 3 criteria for assessing the model: (1) Statistical
132 evaluation using the 'model skill score' (M-score) (Watterson, 1996) – —a non-dimensional measure calculated using
133 location-dependent comparisons between the model and an iodine ocean observation data compilation. (2) Graphical
134 comparison of modeled and observed iodine across 3 illustrative iodine speciation gradients (depth profiles from
135 multiple ocean basins, latitudinal transects of surface waters, and across transects of the Eastern Tropical North Pacific
136 oxygen minimum zone (Moriyasu et al., 2020)). (3) Model applicability to ancient settings by comparing (also using
137 the M-score) projections of ocean surface ~~I:Ca~~I/Ca with published ~~I:Ca~~I/Ca data from the Cretaceous (Zhou et al.,
138 2015).
139

2. Model Description

2.1 The cGENIE Earth system modelling framework

cGENIE is a class of model known as an 'Earth system model with intermediate complexity' (EMIC) – a global climate-carbon cycle model that simplifies one or more (typically physical ~~climatic~~climate) components of the Earth system. In the case of cGENIE, ocean circulation is solved for on a relatively low-resolution grid (here: an equal area 36×36 grid, which equates to 10° in longitude and latitude increments from 3° near the equator to 20° near the poles, and with 16 non-equally spaced vertical levels). This is coupled to a 2D energy-moisture-balance-model (EMBM) and a 2D dynamic-thermodynamic sea-ice model. The physics are described in (Marsh et al., 2011; Edwards and Marsh, 2005). ~~We use a parameter calibration of seasonal pre-industrial climate following Cao et al., (2009).~~

~~The~~ Representation of the primary factors controlling the oceanic iodine cycle – specifically, biological productivity, remineralization, and water column redox – follow Crichton et al., (2021) ~~Crichton et al., 2021~~. In this configuration, ~~are all represented in the model and described in Ridgwell et al., (2007). In that particular configuration,~~ the rate of organic matter export from the ocean surface is calculated based on just a single nutrient (phosphate) control (together with modifiers reflecting ambient light ~~and,~~ sea-ice cover, and temperature) and assumes a Redfield-ratio stoichiometry (1:106) with carbon (Fig. 1). Organic matter is ~~split~~ partitioned into particulate (POM) (33% of total export) and dissolved form~~s~~ (DOM) (67%), with the former sinking down through the water column where it is progressively remineralized ~~according to a prescribed fixed 'decay' curve~~at a rate scaling with ambient temperature ~~, while the latter is physically transported by circulation and decays (is remineralized with a lifetime of 0.5 years). Here, we deviate from Ridgwell et al., (2007) (as well as the calibrated seasonal configuration of Cao et al., 2009) by adopting a calibrated temperature-dependence to both export production as well as the decay of POM in the water column~~ (described in Crichton et al., 2021 and Boscolo-Galazzo et al., 2021). When dissolved oxygen nears depletion, sulphate (SO_4^{2-}) is assumed to be consumd as an electron acceptor ~~supporting~~ to support the remineralization of organic matter (both POM and DOM)~~.~~. The rate of POM remineralization in the water column is governed only by ambient temperature which, in conjunction with a prescribed sinking rate, deterines the vertical distribution of solute release and oxidant consumption. The relative availablity of dissolved O_2 vs. SO_4^{2-} determines the proportion of organic matter degraded by each electron acceptor. In this, ~~the rate of which is governed by a~~the relative consumption of SO_4^{2-} is governened by a SO_4^{2-} half-~~saturaion~~ saturation limitation term as well as a dissolved oxygen (O_2) inhibition term, while ~~the rate that~~ of oxic resperation of organic matter is restricted by an [O_2] half-saturaion limitation term (~~as~~ described in Reinhard et al., 2020). ~~This deviates from the framework described in Ridgwell et al., (2007). The difference is that, here, SO_4^{2-}~~Sulphate can ~~hence~~ be consumed even before dissolved oxygen can become fully depleted. ~~Ambient temperature dictates the total fraction of POM that decays through both pathways per unit time and within each ocean depth layer (Crichton et al., 2021), with local [O2] and [SO4^2-] determining the fractional split between alternative pathways (Reinhard et al., 2020).~~ For DOM, ~~the~~ a decay constant (here: 0.5 years) determines the total fraction that ~~decays~~ is remineralized per unit time. It should be noted that currently, there is no published nitrogen cycle in the cGENIE model framework and ~~hence~~ we do not consider nitrate reduction as part of the redox cascade here.

2.2   Marine iodine cycling in cGENIE

In the cGENIE model, iodine is present in three reservoirs: IO_3^- and I^- in the water column, and I^- incorporated in POM (and DOM). We then consider four processes that transfer iodine between these reservoirs (summarized in Figure. 1): (1) IO_3^- reduction in the water column, (2) I^- oxidation (also in the water column), (3) photosynthetic IO_3^- uptake (and assumed intercellular reduction to I^-), and (4) I^- release to seawater during the remineralization of POM (and DOM) (Fig. 1). As dissolved tracersspecies, IO_3^- and I^- are physically transported and mixed through ocean circulation (as is I incorporated into dissolved organic matterDOM), whereas iodine in POM settles vertically through the water column. This is effectively the same overall framework as used by Lu et al., (2018). Here In this paper we re-assess this framework against an updated compilation of observed iodine speciation in the modern ocean and develop and test alternative representations of IO_3^- reduction (process (1), "threshold"'threshold''threshold', 'inhibition'"inhibition", and 'reminSO4lifetime'"reminSO4lifetime") and I^- re-oxidation (process (2), 'lifetime'"lifetime"'lifetime', 'Fennel'"Fennel"'fennel', and 'reminO2lifetime'"reminO2lifetime"'reminO2lifetime'). Although we describe all 65 different parameterizations below for completeness and a number of different permutations of 3 IO_3^- reduction and 3 I^- re-oxidation processes (presented in S.I.), in this paper we will focus primarily on a single reduction parameterization ('threshold') in combination with the 3 different re-oxidation schemes.

2.2.1 IO_3^- reduction schemes

- **'threshold'.** In the numerical scheme of Lu et al., (2018), when $[O_2]$ falls below a set concentration threshold, IO_3^- is immediately and quantitatively reduced to I^- (thereafter, we term this iodate reduction parameterization "threshold"'threshold').

- **'inhibition'.** The "inhibition"'inhibition' scheme links the IO_3^- reduction rate with the ambient O_2 concentration. Following the formulation for the rate of SO_4^{2-} reduction in Reinhard et al., (2020), we apply an oxygen inhibition term governed by a half-saturation constant. In devising this scheme, we note that while IO_3^- reduction rates have been determined experimentally, the quantitative relationship with $[O_2]$ (or other parameters) is unknown. The IO_3^- reduction under "inhibition"'inhibition' is mathematically described as:

$$d[IO_3^-]/dt = [IO_3^-] \times k_{red} \times \frac{k_{O_2}}{k_{O_2}+[O_2]} \tag{1}$$

in which k_{red} is the maximum first-order reduction rate of IO_3^-, and k_{O2} is the half-saturation constant of O_2.

- **'reminSO4lifetime'.** Reduced sulfur (e.g. sulfides) is also suspected to play an important role in IO_3^- reduction in seawater, especially in the sulfidic zones (Jia-zhong and Whitfield, 1986; Luther and Campbell, 1991; Wong and Brewer, 1977; Truesdale et al., 2013). We therefore devise a scheme ('reminSO4lifetime'"reminSO4lifetime") that scales a nominal 'lifetime' for IO_3^- with the rate of SO_4^{2-} reduction in the model. This has the effect of increasing the rate of IO_3^- reduction (a shorter lifetime) under conditions of higher sulphate reduction rates and hence lower ambient oxygen concentrations and/or higher rates of organic matter degradation:

$$d[IO_3^-]/dt = [IO_3^-] \times \frac{1}{\tau_{sul}} \times d[SO_4^{2-}]/dt \tag{2}$$

in which τ_{sul} defines the rate constant parameter linking the IO_3^- and SO_4^{2-} reduction, while the $d[SO_4^{2-}SO_4]$ is amount of SO_4^{2-} reduced during each model timestep.

2.2.2 I^- oxidation schemes

7

- **'lifetime'.** In Lu et al., (2018), I^- is oxidized to IO_3^- following first-order kinetics regardless of ambient O_2 (scheme ~~"lifetime"~~'lifetime'). In this scheme, I^- oxidation follows the first-order reaction kinetics:

$$d[I^-]/dt = [I^-] \times \frac{1}{\tau} \tag{3}$$

where τ is the lifetime of I^- in seawater.

- **'Fennel'.** Given the overlapping redox potential between I and N (e.g. Rue et al., 1997; Cutter et al., 2018), we explore the potential for a link between areas of I^- and nitrification. To simulate this, ~~Given the potential link between I^- and nitrification,~~ we devise an alternative 'Fennel'~~"Fennel"~~~~'fennel'~~ scheme, in which I^- oxidation rates vary as a function of ambient O_2, increasing with ambient O_2 concentrations towards some hypothetical maximum value following Michaelis–Menten kinetics (Fennel et al., 2005). In Fennel et al., (2005), this parameterization was originally devised for ammonia reoxidation. The form of this response is defined by the maximum reaction rate and O_2 half-saturation constant (Fennel et al., 2005):

$$d[I^-]/dt = [I^-] \times k_{ox} \times \frac{[O_2]}{k_{fenn}+[O_2]} \tag{4}$$

in which k_{ox} defines the maximum rate constant of I^- oxidation, while k_{fenn} is the O_2 half-saturation constant.

- **'reminO2lifetime'.** Finally, in 'reminO2lifetime'~~"reminO2lifetime"~~~~'reminO2lifetime'~~, we associate I^- oxidation with O_2 consumption during remineralization. The logic behind this parameterization is the recent observation of I^- oxidation to IO_3^- catalyzed by bacteria, perhaps in association with ammonia oxidation (Hughes et al., 2021). Although the nitrogen cycle is not currently included in cGENIE, the NH_4^+ oxidation can be scaled to OM remineralization (Martin et al., 2019) and hence to O_2 consumption during remineralization. Under 'reminO2lifetime'~~"reminO2lifetime"~~~~'reminO2lifetime'~~, the lifetime of I^- oxidation is inversely linked to O_2 consumption so that faster remineralization —which in the ocean leads to more intensive NH_4^+ oxidation — enhances I^- oxidation. This I^- oxidation scheme follow this equation:

$$d[I^-]/dt = [I^-] \times \frac{1}{\tau_{O2}} \times d[O_2]/dt \tag{5}$$

where τ_{O2} is the rate constant parameter and $d[O_2]$ is the O_2 consumption during remineralization during a single timestep in the model.

2.2.3 Biological reduction pump

The final pair of coupled processes in the marine iodine cycle framework concerns the processing of iodine directly through the biological pump. Phytoplankton-absorbed iodine is stored in the cell as IO_3^-, I^-, or other forms, followed by release during senescence (Hepach et al., 2020). While there is some uncertainty as to whether IO_3^-~~iodate~~ reduction is assimilatory or dissimilatory (Hepach et al., 2020), we adopt a comparable approach to nitrogen cycling (sequence: NO_3^- uptake, N incorporation into organic matter, remineralization and release as the reduced NH_4^+ form). We assume that~~it is necessary to clarify here that in order to~~we simplify the simulation, the modeled by assuming the IO_3^- tracer is assimilated by phytoplankton and incorporated into POM during photosynthesis ~~In this, IO_3^- is taken up by phytoplankton and incorporated into OM during photosynthesis~~ (Elderfield and Truesdale, 1980) ~~before being~~and released as I^- during remineralization and/or cell senescence (Wong et al., 2002; Hepach et al., 2020; Wong et al., 1985). cGENIE simulates these processes ~~as a function of a~~via an assumed 'Redfield-ratio' of iodine to carbon (I:C

8

248 ratio) in OM. We note that while ~~the value of~~ I:C ~~can be adjusted in the model~~is tunable, it is ~~fixed~~ currently assumed

249 fixed in value throughout the ocean. We discuss the merits of an optimized and uniform I:C compared to variable I:C

250 (e.g., Wa~~d~~dley et al., 2020) in more detail in the discussion.

2.3 Model-data ~~comparison~~evaluation

252 ~~We used the model skill measure (M) (Watterson, 1996) to assess the performance of the marine iodine cycle in~~

253 ~~cGENIE. A major advantage of the M-score is that it is calculated through location-dependent comparison (Fig. 2; Lu~~

254 ~~et al., 2018). Another advantage of the M score is that it captures overall improvement of model performance relative~~

255 ~~to model-minus-observation maps, since it is non-dimensional, and the higher M stands for better performance.~~ For

256 ~~comparison~~ evaluating the marine iodine cycle in the cGENIE model~~with simulated distributions of iodine speciation~~,

257 we compiled oceanic iodine observation data from the literature (Fig. 2~~B~~; Table S4). ~~This~~ Our dataset ~~includes~~ builds

258 on ~~the~~ ~~compiled dataset~~compilation of Chance et al., (2019) ~~and Sherwen et al., (2019)~~, which was used to calibrate

259 the Wadley et al., (2020) model, but includes more recent publications (referenced in Table S4) and is also expanded

260 to include the deep ocean and ODZ data. To avoid the influence of freshwater dilution and recycled iodine from the

261 sedimentary flux, we applied a filter which only keeps the measurements with total iodine (or IO_3^- plus I^-) between

262 450 nM and 550 nM in the dataset. Note that the I^- measurements from the GP16 cruise in the ETSP are not included

263 for the comparison because of potential method considerations (see Cutter et al., 2018 and Moriyasu et al., 2023).

264 After ~~these filtration methods~~filtering, the data were ~~re-~~gridded ~~by taking the average values according~~ to the cGENIE

265 model ~~grids~~grid.

266 We used the model skill measure (M-score) (Watterson, 1996) to assess the performance of the marine iodine

267 cycle in cGENIE compared to the gridded data. ~~A major advantage of the M-score is that it is calculated through~~

268 ~~location-dependent comparison (Fig. 2; Lu et al., 2018). Another advantage of the M score is that it captures overall~~

269 ~~improvement of model performance relative to model-minus-observation maps, since it is non-dimensional, and the~~

270 ~~higher M stands for better performance.~~For each iodine speciation (hereby IO_3^- and I^-), a ~~M score~~M-score value is

271 calculated through comparing ~~re-gridded~~gridded observations versus model results in each corresponding grid (Figure

272 2). The synthesized ~~M score~~M-score for iodine of each model experiment is calculated through averaging those for

273 both I^- and IO_3^-. The higher the M-score value the better the model-data performance.

274

9
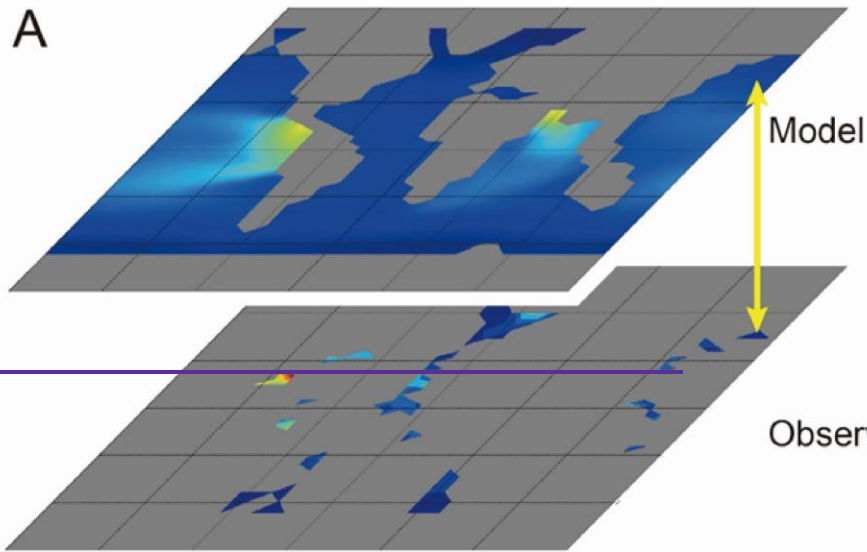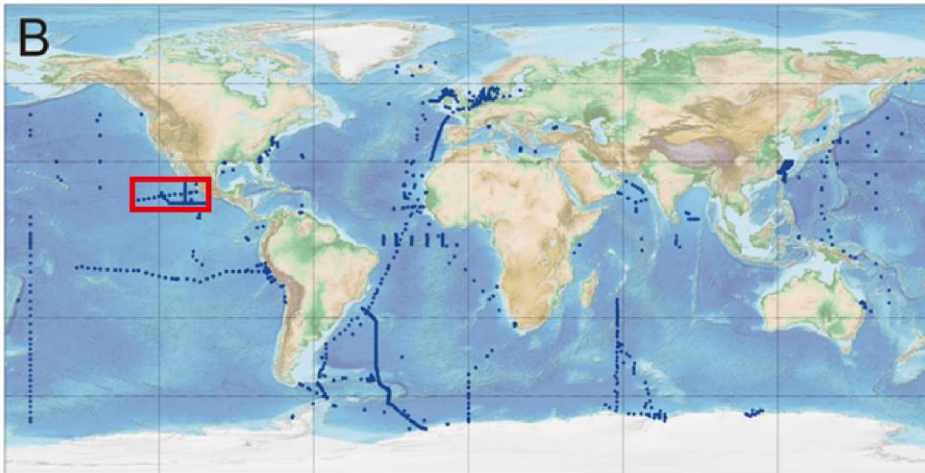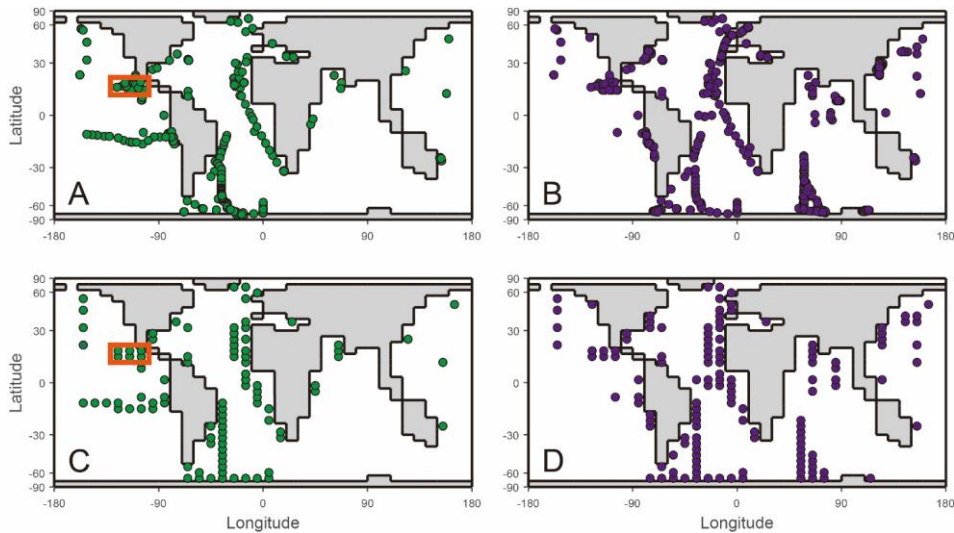
Figure 2: ~~A). An example of location-dependent comparison between I⁻ distributions in the cGENIE model iodine data array and the regridded ocean observation. B). The sampling locations of iodine observation data used for model-data comparison. Some coastal stations included in the figure are filtered out in the model-data comparison. The ETNP transect associated with Fig.6 is labeled as red box.~~ The Ocean surface (uppermost ~81 m corresponding to the depth of the surface layer in the cGENIE model) sampling locations of IO_3^- (A) and I⁻ (B) field observations after data filtration for freshwater and sediment fluxes. The filtered observations were then ~~re~~gridded according to the cGENIE 36×36×16 framework for model-data comparison of IO_3^- (C) and I⁻ (D). The orange boxes in A and C ~~surround~~highlight the grids of ~~ETNP~~the oxygen deficient zone transect shown in ~~Fig. 6~~Fig. 7.

2.4   Sensitivity analyses and model implementation

Because the relative roles of IO_3^- reduction, I⁻ oxidation, and the shuttling of iodine through the biological pump~~IO_3^- planktonic uptake in the water column~~ are uncertain, we calibrate the parameters controlling these processes in cGENIE by creating an ensemble of different parameter value combinations ~~arranged~~ controlling IO_3^- reduction and I⁻ oxidation in a 2D regularly -spaced grid and then repeat the same 2D parameter ensemble for different assumptions ~~of~~ regarding the biological pump (I:C) (Table 1, ~~Fig. 3~~Fig. 4). ~~The output of each ensemble member is then statistically compared to our observational database. We assume the associated parameterization when the model reaches the best M score of replicating modern ocean iodine distribution would also be applied to simulate iodine cycling in the past.~~ We focus on parameter ensembles testing the 3 different parameterizations for I⁻ oxidation (but only 'threshold' as the IO_3^- reduction parameterization) – 'lifetime-threshold', 'fennel-threshold', and 'reminO2lifetime-threshold'. (The results of 2 additional parameterization-combinations – 'lifetime-reminSO4lifetime', and 'lifetime-inhibition' are given in Table S1.) We discuss the reasons for selecting these specific parameterization-combinations in the Discussion section. Finally, ~~To~~to explore whether ~~the~~ the~~c~~GENIE model--simulated dissolved oxygen distribution

300 impart~~ed~~s any particular bias to the tuned iodine cycle, we repeated the model ensembles for each of the 3
301 parameterization-combinations but~~,~~ continually restoring the 3D pattern of [O_2] in the model to that of the World
302 Ocean Atlas 18 (WOA18) climatology (Garcia et al., 2018). The model ensembles are summarized in Table 1.

303   Each ensemble member was run for a total of 2,000 years and each starts from the same initial state, which
304 was an experiment run for 10,000 years to equilibrium using a random set of iodine parameters within the ranges in
305 Table 1. Running ~~the models~~each ensemble member for 2000 years minimizes the CPU time but was also found to be
306 more than sufficient to allow iodine inventories to equilibrate to new steady states. ~~To explore whether the model~~
307 ~~simulated dissolved oxygen distribution imparted any particular bias to the tuned iodine cycle, we repeated the model~~
308 ~~ensembles, continually restoring the 3D pattern of [O₂] in the model to that of the World Ocean Atlas 18 (WOA18)~~
309 ~~climatology (Garcia et al., 2018).~~ The output of each ensemble member is then statistically compared to our
310 observational database.

311

312 **2.5 Evaluation against geological observations**

313 Parameter tuning, and the ability to reproduce modern observations, does not by itself offer any guarantee that spatial
314 patterns are being simulated for the 'correct' mechanistic reason ~~(i.e., specific set and relative importance of~~
315 ~~mechanisms)~~. This is even more pertinent in the context of the application of a modern-tuned model to paleo-redox
316 reconstruction. To ~~test whether our~~quantify to what degree the calibrated parameterization-combinations for the
317 modern marine ~~new~~ iodine cycle ~~had~~have predictive power in the geological past, we carried out a deep-time
318 plausibility test.
319   For the paleo plausibility test, we adopted the Cretaceous, pre-OAE2 (ca. 93 Ma) configuration (continental
320 arrangement and ocean bathymetry, wind stress and velocity, and zonal average planetary albedo boundary conditions)
321 ~~from~~of Monteiro et al., (2012). We choose this particular geological interval because the controls on ocean redox have
322 been previously evaluated using the cGENIE model (Monteiro et al., 2012; Hülse et al., 2019), the oceanic conditions
323 are much more extensively dysoxic and anoxic than present-day and hence represent a relatively severe test of the
324 model iodine cycle, and ~~a~~ number of ~~I:Ca~~I/Ca proxy measurements are available (Zhou et al., 2015). In order to
325 evaluate the same configuration of the iodine cycle as optimized in this study, we also substituted the temperature-
326 independent representation of biological export production and fixed remineralization profile of POM in the water
327 column (i.e., Ridgwell et al., (2007)) for the temperature-dependent scheme of Crichton et al., (2021) used in our
328 modern calibration. However, in substituting the biological pump scheme in the model we ~~change~~alter the ocean redox
329 landscape compared with ~~e.g.,~~ Monteiro et al., (2012). We therefore ~~test~~explore a range of different assumptions
330 regarding the ocean PO_4 inventory at the time as a means of generating a range of different plausible states of ocean
331 oxygenation. In this, we test: 0.2, 0.4, 0.6, 0.8, 1.0, and 1.5 times the mean modern concentration (2.15 μM). We run
332 the model with each of the best-fit (highest M-score) sets of parameter values associated with the main 3~~5~~ different
333 parameterization-combinations (~~but focus on the results of the same 3~~2 additional parameterization-combinations ~~we~~
334 ~~did for comparison against modern~~were run and are presented in SI), and for each of the varying PO_4 inventory
335 assumptions, and for 10,000 years to steady-state. Major cation concentrations were adjusted to a value more

Formatted: Indent: First line: 0.5"

Formatted: Font: Symbol

336 representative of the earlier Cenozoic (18.2 mM [Ca^{2+}], 29.9 mM [Mg^{2+}]) (Panchuk et al., 2008) (Panchuk et al., 2008)

337 although that does not affect the calculation of carbonate I/Ca values. In the absence of independent constraints on the

338 Cretaceous total dissolved iodine inventory, we assumed this to be modern (500 nM mean concentraion).
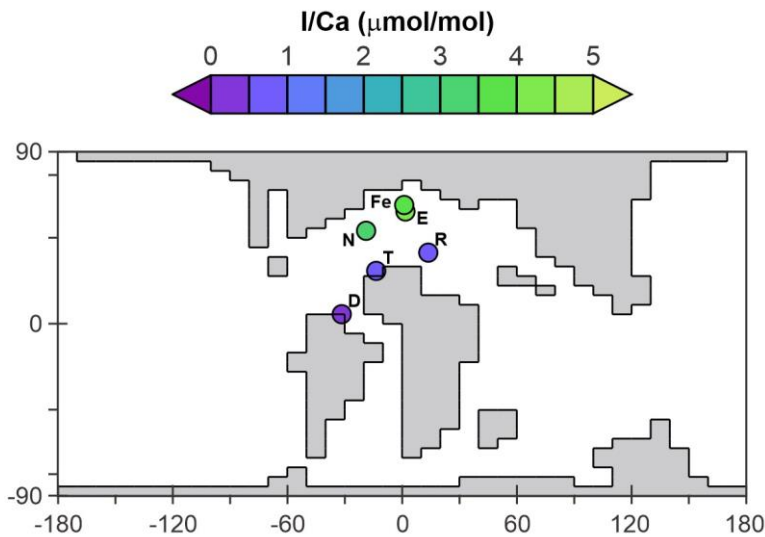
339

340

341

342 **Figure 73: The continental setting during the Cretaceous OAE2 (Cenomanian - Turonian) in cGENIE. The**
343 **colored dots represent averaged pre-OAE2 I/Ca measurements from each of the sections. D = Demerara Rise;**
344 **E = Eastbourne; Fe = South Ferriby; N = Newfoundland; R = Raia del Pedale; T = Tarfaya.**

345

346 The I/Ca data used for comparison with the model come from 6 sections (Zhou et al., 2015, Fig. 7 Fig. 3,

347 listed in Table S3). The pre-OAE2 I/Ca baseline value from each section is estimated through averaging the pre-CIE

348 I/Ca measurements from Table S1 of Zhou et al., (2015). Diagenesis of carbonate hosted I/Ca tends to lower the

349 primary values (Hardisty et al., 2017). However, such an offset is hard to quantitatively predict based on our current

350 knowledge. In addition, according to Zhou et al., (2015), from which we adopted the I/Ca data, most of the sections

351 only suffered minor diagenesis. To simplify the Cretaceous I/Ca-to-IO_3 conversion, we regard the measured I/Ca as

352 primary and acknowledge there is potential uncertainty. For quantitative comparison between the model and the I/Ca

353 data, we create an empirically derived forward proxy model for I/Ca. In this, we took the simulated concentration of

354 IO_3^- and Ca^{2+} in the ocean surface layer of the model at every ocean grid point, and applied the temperature-dependent

355 linear incorporation relationship derived from inorganic calcite synthesis experiment of Zhou et al., (2014), to estimate

356 I/Ca. Specifically, the distribution coefficient (K_D) between I/Ca and [IO_3] (K_D = (I/Ca)/ [IO_3]) shows linear

357 dependency with temperature (Fig. S3 in Zhou et al., 2014). For our Cretaceous model calibration, we apply the K_D

358 based on local temperature (at each grid point associated with a sampling section) simulated by cGENIE. Beyond

359 temperature, we acknowledge that IO_3^- incorporation into carbonate lattice through substitution $IO_3^- + Na^+ \leftrightarrow CO_3^{2-}$

360 $+ Ca^{2+}$ is controlled by $[Na^+]$, $[CO_3^{2-}]$, and $[Ca^{2+}]$ (Podder et al., 2017). However, either quantifying these ions during

361 the Cretaceous seawater or quantitative calculation of ion substitution dynamics requires further constraints. Although

362 uncertainties are inevitable, we assume our temperature-controlled $[IO_3^-]$-to-I/Ca conversion based on current

363 quantitative knowledge meets the requirement for Cretaceous model-data comparison. We extracted simulated I/Ca

364 values from the model grid points corresponding to the sections reported by Zhou et al., (2015) and calculated the M-

365 score.

366
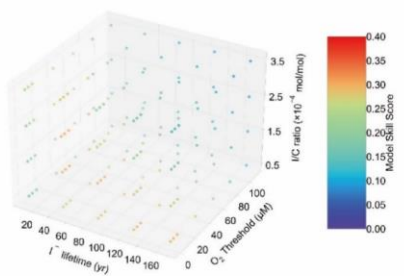
14

367

15
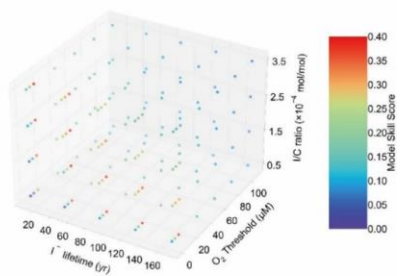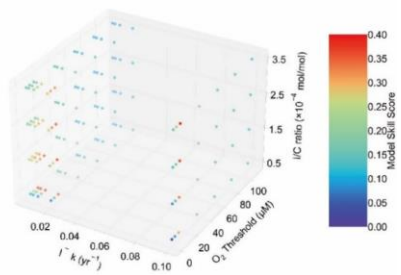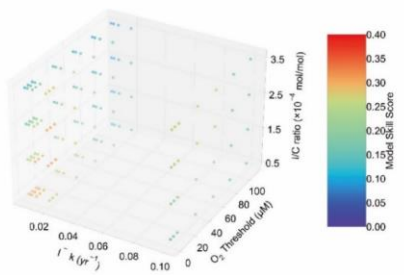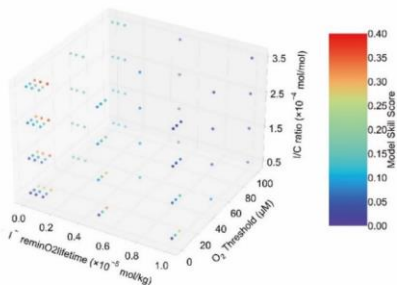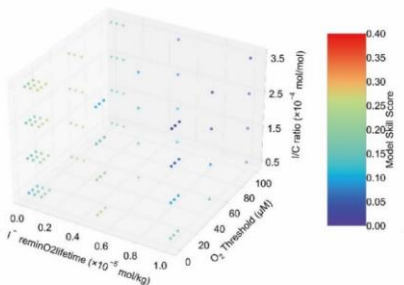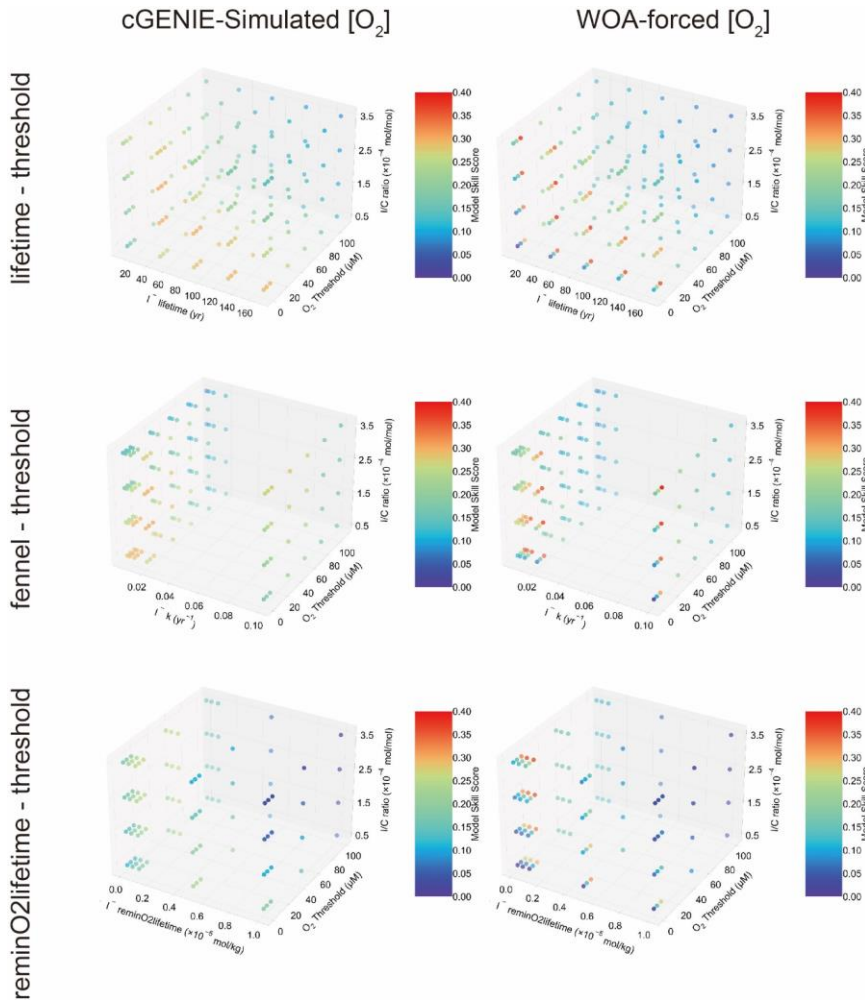
Figure ~~3~~4: The three-dimensional model skill score array of the experiment ensembles.

We ran model ensembles to test five different combinations of iodine cycling parameterizations — ~~"lifetime threshold"~~'lifetime threshold', ~~"Fennel threshold"~~'fennel threshold', and ~~"reminO2lifetime threshold"~~'reminO2lifetime threshold', "lifetime reminSO4lifetime", "lifetime inhibition" (Table S1). While the results for all parameterization combinations are given in the supplement, we only focus on 3 parameterization combinations here (Table 1) — ~~"lifetime threshold"~~'lifetime threshold', ~~"Fennel threshold"~~'fennel threshold', and

Table 1. The cGENIE iodine redox options and the associated range of parameters of these options. The detailed introduction of each parameter is described in section 2.2.2 and the plausibility of these parameter ranges is discussed in 4.1.1. Note that the oxidation rate constant k in 'Fennel' is in unit of year^{-1} in the model configuration, which is the reciprocal of the 'lifetime'. A detailed table containing all considered parameterization ranges can be found in Table S1.

Parameterization-combination Parameter description		Iodine oxidation parameters			Iodine reduction parameters	I:C ratio (× 10^{-4} mol/mol)
		'lifetime' (years)	'reminO2lifetime' (× 10^{-5} mol/kg)	'Fennel' (Inhibition constant/ µM O$_2$)	'threshold' (µM O$_2$)	
Simulation 'lifetime-threshold' 1	cGENIE O$_2$	10-170	\	\	1-110	0.5-3.5
	WOA	10-170	\	\	1-110	0.5-3.5
'fennel-threshold' Simulation 2	cGENIE O$_2$.	10-170 (1/k)	0.01-1	20	1-110	0.5-3.5
	WOA.	10-170 (1/k)	0.01-1	20	1-110	0.5-3.5
'reminO2lifetime-threshold' Simulation 3	cGENIE O$_2$	\	0.01-1	\	1-100	0.5-3.5
	WOA	\	0.01-1	\	1-100	0.5-3.5

384

3. Results

In this section, we start by summarizing the overall statistical outcome of the tuning, then present a series of spatial analysis comparisons for each of the highest M-score ensemble members. The spatial analyses progressively reduce in scale, moving from global surface distributions (Section 3.2), to global and basin-specific water column profiles (Section 3.3), and finally to spatial comparisons for a specific ODZ region (Section 3.4). Our ~~last~~final ~~comparison~~set of results (Section 3.5) ~~is based on~~are of the modeled ~~OAE-2~~Cretaceous scenarios using the best parameterizations from the modern, which then are compared to carbonate ~~I:Ca~~I/Ca ~~data~~values measured in the rock record.

3.1. Model skill score

The M-score values achieved across the complete ensemble for each of the 3 main parameterization-combinations are ~~illustrated~~ shown in ~~Fig. 3~~Fig. 4. ~~The sensitivity test shows the~~ and illustrate how the statistical fit is ~~M score~~M-scores ~~are~~ sensitive to all three of the main parameters ~~for the ensembles in Fig. 3~~. Higher model skill scores are usually reached when ~~"threshold"~~'threshold' is tuned to 10 μM [O_2] for all the ensembles, including both model-simulated [O_2] and WOA-forced [O_2]. For the ensembles, ~~"lifetime threshold"~~'lifetime-threshold' and ~~"Fennel threshold"~~'fennel-threshold', the highest ~~M score~~M-scores are similar— – 0.305 and 0.308, respectively (Table 2). Both these ensembles have the highest performance when ~~"threshold"~~'threshold', ~~"lifetime"~~'lifetime', and I:C ratio are tuned to 10 μM [O_2], 50 years, and 1.5×10^{-4} mol/mol, respectively, which is generally consistent with observations (Lu et al., 2016, 2020b; Tsunogai, 1971; Elderfield and Truesdale, 1980) (discussed in more detail later). The model performance of ~~"reminO2lifetime threshold"~~'reminO2lifetime-threshold' is less good than the other two combinations, with the best ~~M score~~M-score of 0.266 when ~~"threshold"~~'threshold', ~~"reminO2lifetime"~~'reminO2lifetime', and I:C ratio are tuned to 10 μM O_2, 1×10^{-6} mol/kg, and 3.5×10^{-4} mol/mol, respectively (Table 2, ~~Fig. 3~~Fig. 4). We note that for each parameterization-combination, the highest possible ~~M score~~M-score achievable by tuning improves when [O_2] is forced to that of the World Ocean Atlas 18 (WOA18) climatology (Garcia et al., 2018). ~~'reminO2lifetime''reminO2lifetime''reminO2lifetime threshold'~~

3.2. Meridional surface I⁻ distribution

Figure ~~4~~5 shows a comparison between the observed latitudinal distribution of [I⁻] at the surface and as simulated by the model for each parameterization-combination (for the respective best M-score ensemble member). Note that the observations (Section 2.3) are binned to the corresponding model grid cells and as such, reflect averages over the upper-most 80 m of the water column. This represents a reduction from 1338 to 141 surface ocean data points. We find that the surface ocean [I⁻] in the model shows a trend of increasing values towards low latitudes, broadly consistent with observations (Chance et al., 2014) (~~Fig. 4~~Fig. 5). The ~~"lifetime threshold"~~'lifetime-threshold' and ~~"Fennel threshold"~~'fennel-threshold' show similar latitudinal trends, but both overestimate the surface I⁻ in the mid-low latitudes in the southern hemisphere. The ~~'reminO2lifetime-threshold'"~~ ensemble produces better estimation of meridional surface [I⁻] trend, although overestimates [I⁻] in the tropical surface ocean compared to the other two ensembles (~~Fig. 4~~Fig. 5).

18
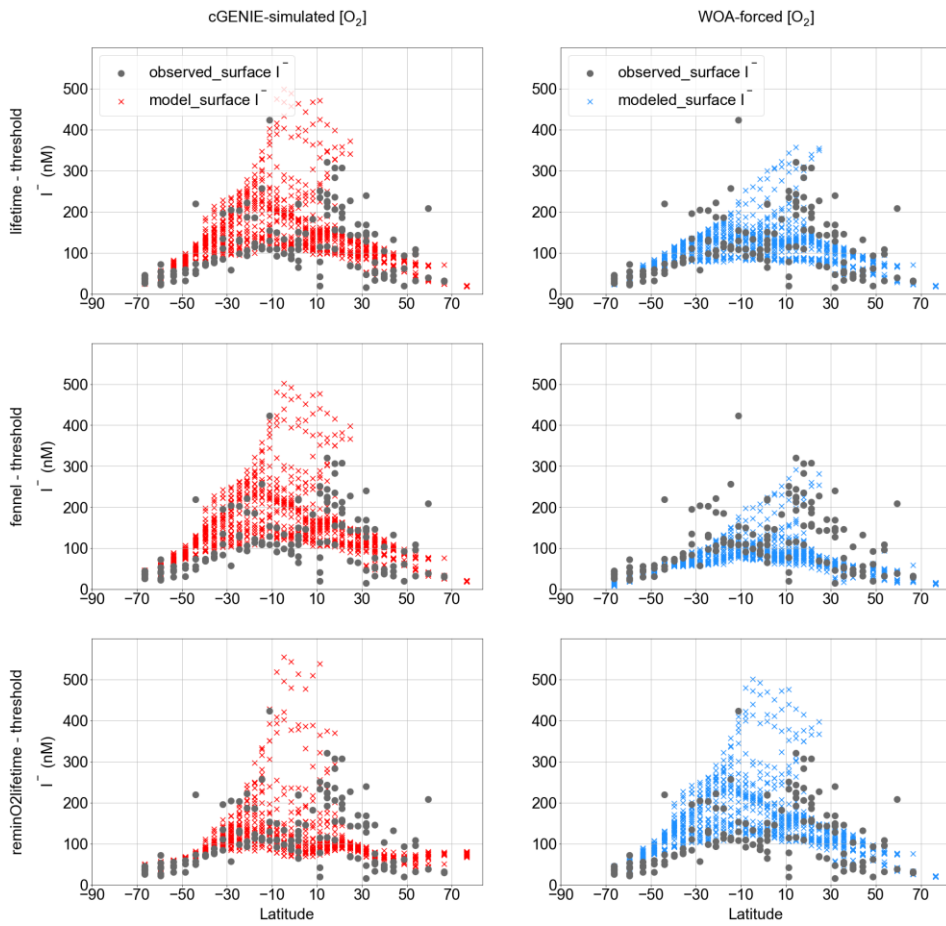
Figure 45: Modeled latitudinal surface iodide distribution compared with observation with the cGENIE simulated [O_2] and the [O_2] restoring forcing. The elevated [I^-] observed and modeled in low latitudes is the result of phytoplankton reduction in the surface ocean. Note that the I^- distribution simulated by "lifetime-threshold" and "fennel-threshold" are close but not identical.

3.3. Global and basin-specific iodine depth distributions

Comparisons between the observed distributions of I^- and IO_3^- seawater concentrations among the global ocean and the Atlantic and Pacific Oceans are presented in ~~Fig. 5~~Fig. 6. Again, we ~~re~~ gridded the iodine observations (see: Section 2.4) and selected sub-sets of the data that lay in either Atlantic or Pacific basins, contrasting with the corresponding model values at those locations. We find only relatively minor differences between the best M-score

431 ensemble member of each of all three parameterization-combinations, and all show increased [IO$_3^-$] and decreased [I$^-$]

432 with increased depth below the photic zone in the Atlantic and Pacific basins, as well as globally (Fig. 5Fig. 6). The

433 modeled depth profile broadly matches with observation in the Atlantic and deep Pacific Ocean, except the

434 underestimated subsurface peak of [I$^-$] observed in the Pacific and overestimated [IO$_3^-$] in the deep Pacific (Fig. 5Fig.

435 6). This mismatch of subsurface I$^-$ peak is probably the result of sampling bias, with most of the Pacific iodine

436 observations from ODZs in the Eastern Tropical North Pacific (ETNP) and the Eastern Tropical South Pacific (ETSP).

437 For example, in model depth profiles masked to only include grid points with corresponding observations, the

438 modelled Pacific depth profiles show a clear mid-depth ODZ feature (Fig. S8S9).

439

440
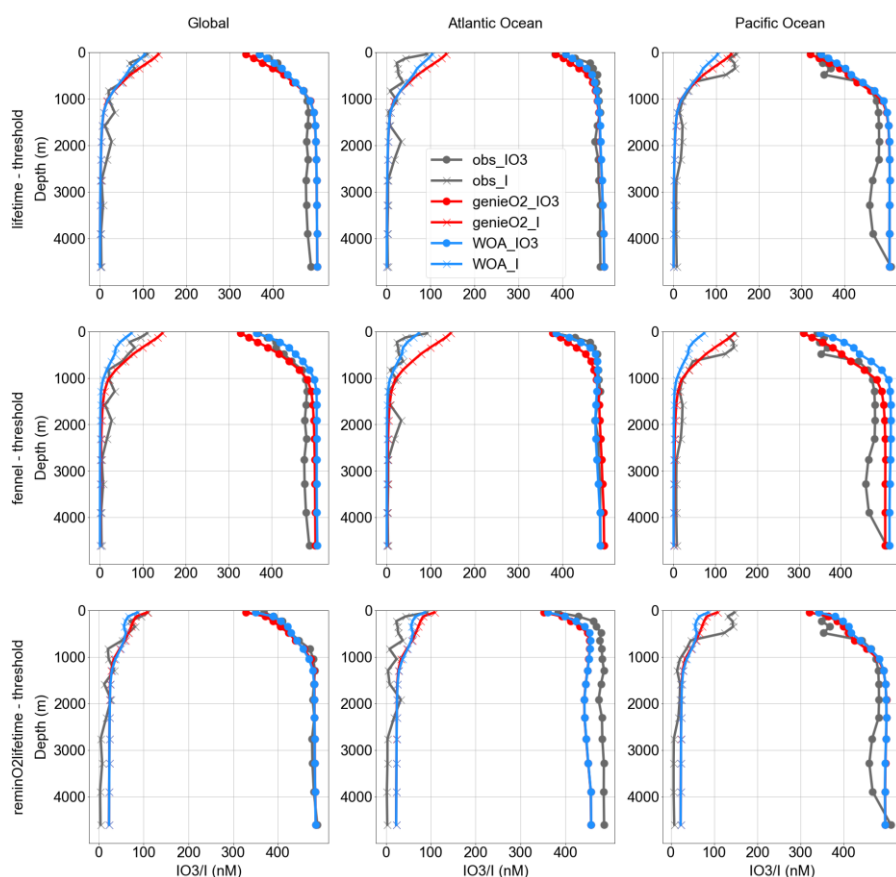
Figure 56: Modeled averaged iodine (including iodate and iodide) depth profile among global ocean, the Pacific, and, the Atlantic compared with observation. The surface I$^-$ enrichment among the ocean basins is caused by phytoplankton reduction. The subsurface (~500m) I$^-$ enrichment is the result of sampling bias that since most of the observations are from the ETNP and ETSP ODZs (see main text for details).

20

445

3.4.   Iodine distribution within ODZs

447   To assess the model ability to simulate iodine cycling in marine low oxygen environments, we compared distributions

448   of oxygen and iodine species in the ETNP (~~Fig. 6~~Fig. 7). The O_2 transects amongst all model simulations are the same

449   because we only changed the parameterizations of the iodine cycle between ensembles and ensemble members (i.e.,

450   they all simulate the same biological pump in the ocean). All the three chosen best-performance-experiments show

451   similar iodine anomalies (IO_3^- depletion) in the ETNP, fitting the general feature of the observation. Other

452   parameterizations did not replicate the ODZ (Fig. S4). However, even under the "best-fitting" parameters, compared

453   to the observations, the ODZ feature in the model is underestimated both in intensity and in areal extent compared to

454   the observations (Fig. 7). Notably, compared to $[O_2]$ measured in the ETNP transect, the model underestimates the

455   extent of the ODZ. Severe deoxygenation below 50 μM $[O_2]$ was observed in relatively shallow depths between 100-

456   200m in the ETNP, and this ODZ extends for more than 3000 km towards off-shore from Mexican coast (~~Fig. 6~~Fig.

457   7). Although cGENIE simulates the O_2-deficient pattern in the ETNP, the extent of the ODZ is underestimated. The

458   simulated oxycline is ~200 m deeper than the observation and the $[O_2]$ variation is gradual. The ODZ below 20 μM

459    $[O_2]$ in the model is limited to a small spatial extent within 1000 km offshore, which is much smaller than that in the

460   observation (~~Fig. 6~~Fig. 7).

461
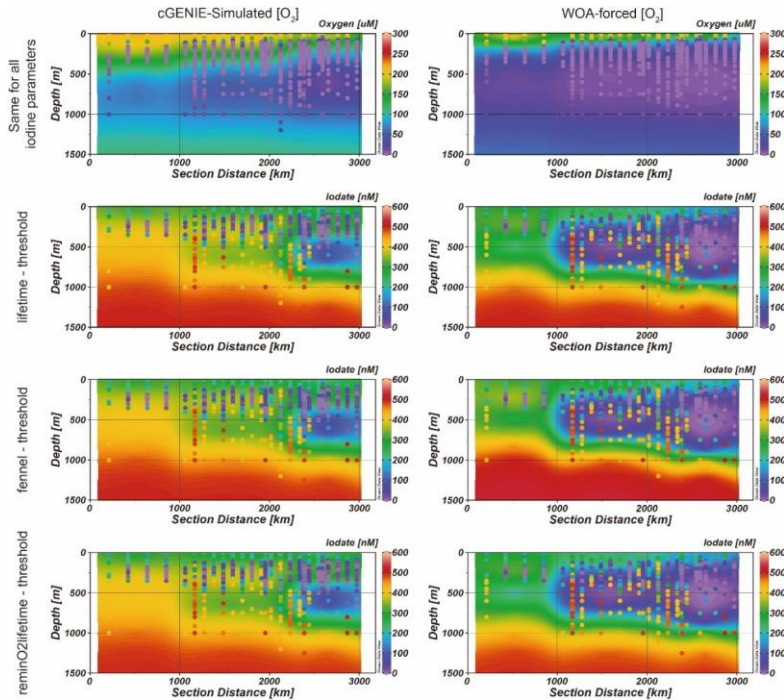
Figure 67: Modeled (contour) and observed (colored dots) west-to-east transect (location shown in Fig. 1) of O_2 (top row) and IO₃⁻ and O₂(bottom rows) in the ETNP. Note that the WOA-forced [O_2] models simulate a larger extent of IO₃⁻ anomaly, which better matches the observation. The left-hand panel contours are model results based on cGENIE-simulated [O_2] while contours on the right are model results from WOA-forced [O_2].

All the three chosen best performance experiments show similar iodine anomalies (IO₃⁻ depletion) in the ETNP, fitting the general feature of the observation. Other parameterizations did not replicate the ODZ (Fig. S4). However, even under the "best-fitting" parameters, compared to the observations, the ODZ feature in the model is underestimated both in intensity and in areal extent compared to the observations (Fig. 6). The observed IO₃⁻ depletion zone ([IO₃⁻] <100 nM) occurs in shallower depths between 100-500 m, matching the shallow ODZ and spans ~2000 km offshore; however, the modeled IO₃⁻ depletion zones in the ETNP are located in 400-700 m, and only extends within 1000 km from the shore.

We also ran model ensembles forcing cGENIE to restore the modern ocean [O_2] annual average climatology to that of the WOA18 (Garcia et al., 2018) (Fig. 6Fig. 7). Now theUnder these conditions, the subsurface IO₃⁻ depletion zone in the ETNP ODZ in all three ensembles extends ~2000 km offshore and spans across 100-1000 m in depth (Fig. 67). The shallow and extended ODZ iodine distribution in the ETNP better matches the observation compared to non-O_2 restoration simulations.

22

481 **Table 2. The performance of the cGENIE iodine simulations and associated parameterization when the**
482 **model reaches the best global ~~M score~~M-score. Note that the oxidation rate constant _k_ in 'Fennel' is in unit of**
483 **year^{-1} in the model configuration, which is also the reciprocal of the 'lifetime'. The full model performance is**
484 **summarized in Table S2. ~~Note that the lifetime in 'Fennel' is parameterized as k (year^{-1}) = 1/lifetime.~~**

Parameterization-combination ~~Parameter description~~		Iodine oxidation parameters			Iodine reduction parameters	I:C ratio (× 10^{-4} mol/mol)	Model skill score
		'lifetime' (years)	'reminO2lifetime' (× 10^{-5} mol/kg)	'Fennel' (Inhibition constant/ μM O$_2$)	'threshold' (μM O$_2$)		
'lifetime-threshold'~~Simulation 1~~	cGENIE O$_2$	50	\	\	10	1.5	0.305
	WOA	50	\	\	10	1.5	0.385
'fennel-threshold'~~Simulation 2~~	cGENIE O$_2$	50 (1/k)	\	20	10	1.5	0.308
	WOA	10 (1/k)	\	20	10	3.5	0.385
'reminO2lifetime-threshold'~~Simulation 3~~	cGENIE O$_2$	\	0.1	\	10	3.5	0.266
	WOA	\	0.1	\	10	3.5	0.365

485

486 ~~**3.5 Ancient iodine: Oceanic Anoxic Event case study**~~ **Evaluation against geological observations**

487

488
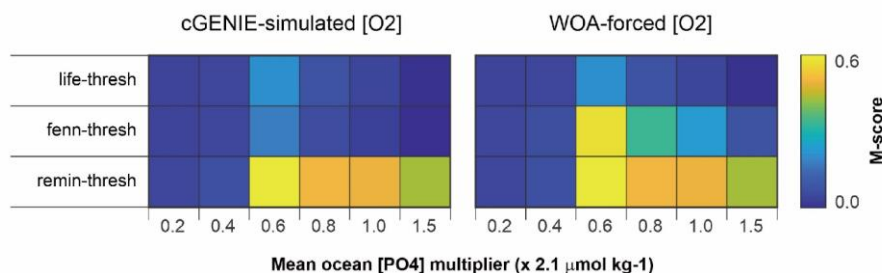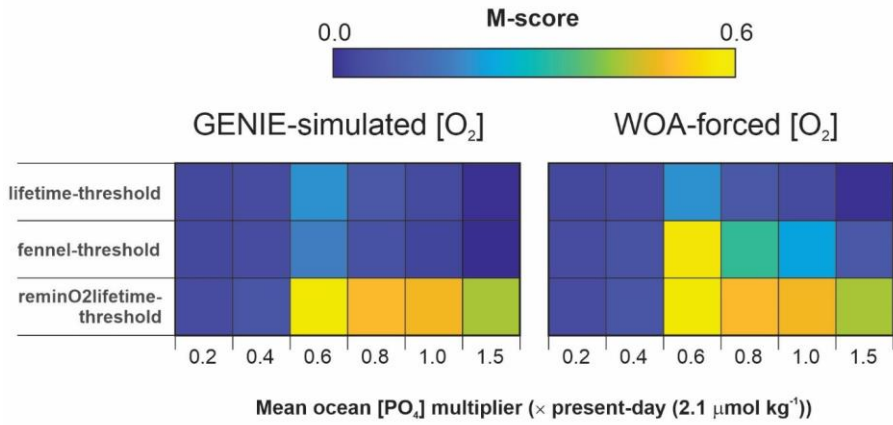
Figure 8. The model skill scores of modeled and measured I/Ca during the pre-OAE2. The iodine cycling parameters are derived from modern simulations with cGENIE-simulated [O$_2$] and WOA-forced [O$_2$], respectively. ~~Parameterization-combination #1 == lifetime-threshold; parameterization-combination #2 = fennel-threshold; parameterization-combination #3 = reminO2lifetime-threshold.~~

The statistical results of the pre-OAE2 evaluation are illustrated in Fig. 8 for the 3 main parameterization-combinations and for parameter calibrations derived from internally and WOA-forced dissolved oxygen distributions (and in Fig. S10 for the full set of parameterization-combinations tested). Most of the parameterization-combinations reach their highest ~~M score~~ M-scores under the assumption of 0.6-0.8 × modern [PO$_4$] (Fig. S10). Previous analysis using the same climatological configuration of the cGENIE model indicated a PO$_4$ inventory of 1.0 x modern was most consistent with geological redox-related observations prior to OAE2 (Monteiro et al., 2012). However, our assumption here of temperature-dependent POM export and remineralization leads to higher export and shallower more intense ODZs compared to temperature-invariant biological scheme (see: Crichton et al., (2021)). Hence, for a similar degree of ocean anoxia, we would expect the need for a slightly lower nutrient inventory, as we indeed find.

In terms of the I/Ca M-score, we find the parameterization-combinations 'reminO2lifetime-threshold' and 'fennel-threshold' better replicate the geological observations compared to the 'lifetime-threshold'. For 'fennel-threshold', the WOA-derived parameter set values differ~~ent~~ from those derived from cGENIE-[O$_2$] (Table 2) and perform better. The performance of the scheme 'reminO2lifetime-threshold' is largely independent of the ocean PO$_4$ inventory assumption for values of 0.6 × modern and higher.

~~To assess the ability of cGENIE to reconstruct the iodine cycle in deep-time, we picked the parameters associated with highest~~ ~~M score~~ M-score ~~in each of the ensembles (Table 2) and ran the model under an~~the OAE2 scenario with variable PO$_4$ (Zhou et al., 2015). We calculated the pre-OAE stage modeled I:/Ca based on the linear relationship between I:Ca~~I/Ca~~ and IO$_3^-$ and temperature from carbonate synthesis experiments (Zhou et al., 2014). Importantly, this relationship is temperature dependent, so the temperature from the relevant model grid point was used for this calculation. The reconstructed I:/Ca from each section (Figure 8) was then compared with the simulated I:/Ca in the corresponding model grid, and the comparisons are presented by the~~ ~~M score~~ M-score ~~(Figures 7, 8, and 9). Note that most of the models reach highest~~ ~~M score~~ M-score~~s under 0.6-0.8× modern PO$_4$.~~

24

4. Discussion

In summary: we ~~ran~~ presented the results of cGENIE Earth system model ensembles (both with internally calculated and WOA-imposed $[O_2]$ distribution) ~~ensembles for five~~ for 3 parameterization-combinations of iodine cycling that showed the best performance ~~parameters~~ (but summarized a total of 5 different parameterization-combinations in Table S2) ~~in the cGENIE Earth system model (both with internally calculated and WOA-imposed $[O_2]$ distribution) and presented the results for 3 of them that showed the best performance~~. We analyzed the performance of the ensembles via: (1) ~~M score~~ M-score for the model-data match of both $[I^-]$ and $[IO_3^-]$ across the entire ocean, (2) qualitative model-observation comparison of latitudinal surface ocean distributions of $[I^-]$, (3) inspection of averaged depth profiles in global and individual ocean basins for both $[I^-]$ and $[IO_3^-]$, (4) inspection of iodine transects across ~~the~~ across the Eastern Tropical North Pacific (ETNP) ODZ, and (5) ~~M score~~ M-score for model and carbonate ~~I:Ca~~ I/Ca observations (Zhou et al., 2015) for ~~pre-OAE2~~ the Cretaceous.

4.1. Overall model skill score comparison

Two broad observations emerge from the ~~M score~~ M-score comparison. First, the 1st-order kinetic iodine oxidation associated ensembles (‘lifetime-threshold’ and ‘Fennel-threshold’) have the highest ~~M score~~ M-scores (Table 2), under both cGENIE-simulated $[O_2]$ and WOA-forced $[O_2]$. This is consistent with previous observations of 1st-order kinetics for I^- oxidation (Tsunogai, 1971). Second, the simulations with WOA-forced $[O_2]$ produce significantly higher ~~M score~~ M-scores than that of the cGENIE-simulated $[O_2]$ field (at least ~0.0 8 of improvement; Table 2). Despite a 1st-order non-O_2 dependent oxidation mechanism providing the highest ~~M score~~ M-scores, the WOA vs internally model-generated dissolved oxygen distributions comparison highlights the O_2 and related redox dependency of the iodine cycle from the perspective of IO_3^- reduction. Each of these factors are discussed in the following Section 4.1.1.

~~Notably, our M score M-score results also demonstrate a potentially minor role, if any, for iodine cycling with DOC. As described in 2.3.1, the "reminO2lifetime"'reminO2lifetime' and the "reminSO4lifetime" scales I~ oxidation and IO_3^- reduction with O_2 consumption and SO_4 reduction during the remineralization of POC (or POC and DOC), respectively. An alternative (with DOC remineralization) scenario was tested to combine the iodine redox reactions with DOC remineralization in cGENIE (Table S1). Compared to the default settings, adding the DOC remineralization control to the I^- oxidation ("reminO2lifetime"'reminO2lifetime') or IO_3^- reduction ("reminSO4lifetime") does not increase the M score M-score of the model. More than the overall M score M-score, the simulation of latitudinal I^- trend in the defaulted no DOC-controlled iodine cycle models performs better in replicating the depth profiles, as well as the IO_3^- depletion feature in the ODZ (discussed in later sections), especially for "reminO2lifetime-threshold"'reminO2lifetime-threshold' ensembles."~~

4.1.1. Parameter value plausibility

A credible representation of the marine iodine cycle requires not only that observations can be replicated, but that ~~replication occurs when~~ in achieving a fit to observations, tuned parameter values fall within real-world ranges. In this

25

552   section, we discuss the ~~validity~~ plausibility of our best-fit (maximized M-score) parameter values. For the iodine cycle,

553   these parameters ~~include~~ are: the O_2 threshold, ~~I:C ratio, and the~~ parameter (depending on the specific

554   parameterization-combination) controlling the I^- oxidation rate, and the cellular I:C ratio.

555   Our model ~~M score~~M-score is highest with an $[O_2]$ reduction threshold of 10 µM (~~Fig. 3~~Fig. 4 and Table 2).

556 Although it is generally well accepted that IO_3^- is reduced in low oxygen settings (Luther, 1991; Rue et al., 1997;

557 Wong et al., 1985; Wong and Brewer, 1977; Farrenkopf and Luther, 2002), the degree of O_2 depletion that triggers

558 IO_3^- reduction is still unclear. A relative~~ly~~ high threshold for triggering IO_3^- reduction ~~is~~ has been proposed based on

559 comparison between planktic and benthic foraminiferal ~~I:Ca~~I/Ca and ambient $[O_2]$ (20-70 µM O_2; Lu et al., 2016,

560 2020a). These $[O_2]$ thresholds are similar to that determined in a previous cGENIE-based iodine cycle study (30 µM)

561 (Lu et al., 2018), but it is difficult to directly compare this to our results because of differences in the model

562 representation of the ocean biological pump, the iodine observational data set, and model-data comparison methods

563 utilized.

564   Many of the studies suggesting a relatively high $[O_2]$ threshold ~~is~~ are based on ~~evaluations~~ the relationship

565 of $[IO_3^-]$ and $[O_2]$ within the upper chemocline of ODZs; however, evaluation of $[O_2]$ and $[IO_3^-]$ from ODZs

566 throughout the entire water column suggest the potential for IO_3^- persistence within the low oxygen cores of ODZs.

567 Specifically, IO_3^- accumulation is observed within the ETNP and ETSP at depths where $[O_2]$ is close to or below the

568 detection limit of the sensors which is reported near 1 µM (Hardisty et al., 2021). In addition, it is worth noting that

569 the kinetics of IO_3^- reduction is heterogeneous both within and between ODZs. For example, a transect evaluating IO_3^-

570 reduction rates in the ETNP observed rapid rates in the upper oxycline, where $[O_2]$ was near ~12 µM, but the potential

571 for sluggish rates in the ODZ cores, where $[O_2]$ was below detection. In an early study of the Arabian Sea, IO_3^- was

572 reduced rapidly within the ODZ core. Together, these suggest IO_3^- reduction may be controlled by factors beyond O_2

573 (Hardisty et al., 2021; Farrenkopf and Luther, 2002). For example, IO_3^- is likely formed in high $[O_2]$, non-ODZ water

574 masses but can be sustained upon transport or mixing within oligotrophic, offshore ODZ regions where organic

575 supplies are more limited (Hardisty et al., 2021). A comparison to the N cycle would also indicate a low $[O_2]$

576 threshold— for example, denitrification has a sub-µM $[O_2]$ threshold and has a similar redox potential with IO_3^-

577 reduction (Dalsgaard et al., 2014; Thamdrup et al., 2012). A sub-µM $[O_2]$ threshold for IO_3^- reduction could explain

578 the $[IO_3^-]$ variations observed in ODZ cores with $[O_2]$ below the µM detection limits of sensors; however, iodine

579 speciation has yet to be analyzed alongside $[O_2]$ measurements via sensors with sub-µM detection limits, such as

580 STOX sensors. Regardless, our 10 µM $[O_2]$ threshold based on maximizing the ~~M score~~M-score reflects a global

581 average value and clearly falls within the ranges of oceanographic observations.

582   For both our study and that of Lu et al., (2018), an I^- lifetime of 50 years maximizes model performance.

583 However, Lu et al., (2018) chose to implement a slightly lower value of 40 years for their paleo-application because

584 it reflected the slowest rate observed in the literature at that time (Tsunogai, 1971). Notably, though IO_3^- is the most

585 abundant marine iodine species, its production from I^- has never been unambiguously observed under normal marine

586 conditions. This has acted as a major hinderance on providing direct constraints. That said, our ~~cGENIE~~ model-based

587 estimate is consistent with a multitude of other constraints that indicate that I^- oxidation to IO_3^- undergoes extremely

588 slow kinetics. The I^- oxidation rates calculated through indirect methods including mass balance and seasonal iodine

589 speciation changes (Tsunogai, 1971; Campos et al., 1996; Truesdale et al., 2001; He et al., 2013; Edwards and

590 Truesdale, 1997; Žic et al., 2013; Moriyasu et al., 2023) or through radiogenic tracer spiked incubations (Hardisty et

591 al., 2020; Schnur et al., 2024; Ştreangă et al., 2024) have a wide range of variation from 1.5 nM/yr to 670 nM/yr. The

592 lifetime in cGENIE is 50 years, which can be approximately converted to the zeroth order rate of <9 nM/yr, falling in

593 the lower end of the previous studies.

594   Our best-fit I:C ratio is 1.5×10^{-4} mol/mol, ~~and this value~~which is in agreement with plankton measurements

595 and mass-balance calculations (Chance et al., 2010; Elderfield and Truesdale, 1980). In the photic zone, IO_3^- is taken

596 up by phytoplankton and incorporated into their cellular structures followed by subsequent conversion into I^- (Hepach

597 et al., 2020). Due to this, it is assumed that IO_3^- removal in the surface layer of the ocean is a function of organic

598 carbon fixation during primary productivity according to Redfield-like ratios (Campos et al., 1996; Chance et al.,

599 2010). Of the parameters incorporated into the model, in theory, I:C should probably be the best constrained. However,

600 published I:C ratios based on field and laboratory measurements vary over several orders of magnitude (10^{-5} to 10^{-3})

601 (Elderfield and Truesdale, 1980; Campos et al., 1996; Hepach et al., 2020; Chance et al., 2010). To limit the number

602 of model simulations and size of the ensembles, we only varied I:C between 5×10^{-5} and 3.5×10^{-4} mol/mol (in

603 increments of, ~~increasing by~~ 1.0×10^{-4}), which covers the range indicated by previous studies (Elderfield and Truesdale,

604 1980).

605   It is unlikely that the I:C value is constant across the global ocean due to differences in phytoplankton

606 composition~~s~~ and other factors, such as temperature (Wadley et al., 2020). In cGENIE, most of the elevated (> 200

607 nM) surface $[I^-]$ values ~~over 200 nM is present~~ occur in the ETSP and the northern Indian Ocean, representing the

608 effect of high primary productivity and transformation of IO_3^- to I^- via the rapid recycling DOM 'loss term' in the

609 representation of biological export in the model (Fig. S6). The ~~mismatch~~ ~~underestimation~~overestimation of tropical I^-

610 with t~~between t~~he model ~~and the observations~~ probably hints that the I:C ratio is not constant in the ocean, as ~~which~~

611 is also hypothesized by Wadley et al., (2020), although in the absence of an explicit representation of primary

612 productivity in the model and ~~lack of a~~ spatially variable f-ratio~~s~~ (Laws et al., 2000) (implicitly, the f-ratio ~~is~~can be

613 considered to be 0.33 everywhere in cGENIE). In testing a fixed, spatially uniform I:C, Wadley et al. (2020)

614 underestimated surface $[I^-]$ in low latitudes and overestimated concentrations in mid-latitudes. Based on their model-

615 observation comparison, they hypothesized that the I:C ratio decreases systematically with sea surface temperature

616 (SST) (Wadley et al., 2020). Until more constraints are developed on spatial variability and associated driving factors

617 for I:C, a generalized approach of a globally uniform I:C remains the most parsimonious assumption, especially

618 considering cGENIE's intended extrapolation to ancient settings.

619 **4.1.2.**   **Comparing alternative iodide oxidation parameterizations in cGENIE**

620 Due to similarity in redox potentials, ~~the~~ iodine cycling in the ocean has been hypothesized to be linked to the cycling

621 of nitrogen (Rue et al., 1997). Nitrification promoting I^- oxidation to IO_3^- has been ~~hypothesized~~ inferred from~~in~~ field

622 studies (Truesdale et al., 2001; Žic et al., 2013), and more recently has been linked via observation of I^- oxidation to

623 IO_3^- by ammonia oxidizing bacteria in laboratory environments (Hughes et al., 2021). We further note that Wadley et

624 al., (2020) explicitly link I^- oxidation to NH_4^+ oxidation in their surface ocean iodine cycle model.

27

Formatted: Indent: First line: 0.5", Don't add space between paragraphs of the same style

625   As an alternative to the first-order lifetime oxidation parameterization used here and in Lu et al., (2018) and
626   in the current absence of a full nitrogen cycle (and hence explicit NH_4^+ oxidation) in cGENIE, we also applied a
627   strategy (~'reminO2lifetime'~) which links I^- oxidation to organic carbon remineralization and the consumption rate
628   of dissolved oxygen. The reasoning behind this is that the O_2 consumption rate in the model implicitly reflects bacterial
629   oxidizing activity in the water column and hence the potential for I^- to be oxidized to IO_3^-.

630   We find that the overall model performance involved with the 'reminO2lifetime' is lower than other
631   experiments where I^- oxidation is ubiquitously oxidized according to a parametrized lifetime, or 'lifetime-threshold'
632   (maximum ~~M score~~M-score 0.266 vs. 0.305/0.308 under cGENIE simulated [O_2]) (~~Fig. 3~~Fig. 4 and Table 2). However,
633   despite slightly lower ~~M score~~M-scores, the 'reminO2lifetime'' scheme generally replicates the latitudinal surface [I^-]
634   trend, the depth profiles in the ocean basins, and the ODZ transect (Figs. 4-6).

635   Under the default 'lifetime' scheme, I^- will oxidize in the whole ocean regardless of the concentration (or
636   even presence/absence) of ambient O_2. This scenario might hence not perform well in replicating the ocean iodine
637   cycling at intervals during the Phanerozoic when ODZs were highly expanded, especially for O_2 lower than the IO_3^-
638   reduction threshold which should inhibit I^- oxidation.~~or particularly during the Precambrian when the majority of the~~
639   ~~ocean was ferruginous or euxinic and highly depleted in O_2 (for example, summarized by Lyons et al., 2014)~~. Ideally,
640   for application ~~to~~ in paleoceanographic studies, I^- oxidation should be linked to ambient ~~an~~ [O_2] ~~related I^- oxidation~~
641   ~~alternate scheme is required~~ in some way. Although thermodynamics theory suggests O_2 does not directly drive I^-
642   oxidation (Luther et al., 1995), field studies in ODZs indeed observed low [O_2] inhibits this process (Farrenkopf and
643   Luther, 2002; Moriyasu et al., 2020). We hence developed and tested variable I^- oxidation kinetics, with the ambient
644   dissolved O_2 providing an inhibition of the rate of oxidation based on the enzymatic nitrification scheme of Fennel et
645   al., (2005).

646   Since most of the ocean is fully oxygenated today, ~~the~~ there is little difference ~~of~~ in ~~M score~~M-scores between
647   ~~'~~'lifetime'' and ''Fennel'' oxidation ~~models are minor~~ parameterizations (0.305 vs. 0.308, Table 2). ~~The parameter~~
648   ~~valuess associated with the highest M score~~M-scores ~~in each between two oxidation options scheme are also very~~
649   ~~close to each other, except with the exception that 'Fennel''Fennel''fennel' oxidation together with the model~~under
650   ~~WOA forcing, has a higher optimal I:C ratio (3.5 × 10^{-4} mol/mol) and faster saturated I^- oxidation kinetics (0.1 yr^{-1} vs.~~
651   ~~0.02 yr^{-1} in other ensembles). The parameter differences between the 'Fennel''Fennel''fennel' WOA ensemble and~~
652   ~~other models ensembles make sense because the faster oxidation rate compensates the increased I^- production through~~
653   ~~the higher biotic uptake rate.~~ Despite the very close M-scores, 'Fennel' oxidation ~~has a~~under WOA-forcing has a
654   higher optimal I:C ratio (3.5~~,~~ × 10^{-4} mol/mol) and faster saturated I^- oxidation kinetics (0.1 yr^{-1} vs. 0.02 yr^{-1} in other
655   ensembles)~~,~~. Such parameter differences between 'Fennel'-WOA and other ensembles reflect compensation between
656   faster oxidation rate (②in Fig. 1) and increased I^- production through the higher biotic uptake rate (③in Fig. 1). The
657   pre-OAE2 simulations are particularly illustrative of this tradeoff and are discussed in more detail in section 4.3.

658   In summary, all the three parameter~~ization~~ combinations produce high and comparable ~~M score~~M-scores
659   and similar parameters (oxidation, reduction, and I:C) associated with these ~~M score~~M-scores (Table 2). Although
660   direct field-based evidence to evaluate the controlling parameters of 'reminO2lifetime' is absent, the parameters
661   controlling the other model scheme are consistent with previous studies.

28

Commented [AR15]: This is not sufficiently clear as to what you are trying to say

Commented [MOU16R15]: Keyi: simplify the text here

Formatted: Superscript

Formatted: Superscript

Formatted: Superscript

Formatted: Superscript

Formatted: Superscript

Formatted: Font: (Default) Cambria Math

4.2.   Beyond the M-score: model-data comparison across iodine gradients

As applied here, the ~~M score~~M-score provides a quantitative measure that describes the overall model global performance and allows us to directly compare the implications of parameter value and parameterization choices. However, ~~the~~ a ~~M score~~M-score based on a global dataset ~~overlooks~~ can obscure regional gradients that may be important for both paleo- and modern oceanographic research. Indeed, amongst all the various ensembles we ran as part of this study (Table S1), only 'lifetime-threshold', "'lifetime-Fennel'", and 'reminO2lifetime-threshold'" performed sufficiently well in replicating the modern oceanic iodine gradients (Figs. S2-S4) ~~and informed our decision~~ ~~to~~that we decided to focus only on these 3 parameterization-combinations ~~here~~. We now discuss this in more detail below.

4.2.1.   Meridional surface [I⁻] gradient

All the 3 main parameterization-combinations summarized in Table 2, as well as the observations, show enrichment of I⁻ in the surface ocean at low latitudes (~~Fig. 4~~Fig. 5). The pathway of transforming IO₃⁻ into I⁻ in these oxidized waters is through primary productivity in the photic zone, which result~~s~~ed in I⁻ accumulation within the mixed layer (Chance et al., 2014). In the low latitudinal surface ocean, weaker vertical mixing resulting from warmer surface temperatures allows I⁻ accumulation in the shallow mixed layer (Chance et al., 2014; Moriyaus et al., 2023). ~~, such vertical mixing feature is also simulated by cGENIE (Fig. S7).The pathway of transforming IO₃⁻ into I⁻ in these oxidized waters is through primary productivity in the photic zone, which is temperature dependent (Chance et al., 2014). A recent north-south transect showed the highest surface I⁻ enrichment in the oligotrophic, permanently stratified tropical stations (Moriyasu et al., 2023).~~ Therefore, the IO₃⁻ flux from deep waters through seasonal mixing may be an important balance to *in-situ* IO₃⁻ reduction rate by primary producers in the high latitudes (Chance et al., 2014; Moriyasu et al., 2023). Importantly, this temperature stratification and related vertical mixing trend is also simulated by cGENIE (Fig. S7). The cGENIE model generates the general pattern of latitudinal surface I⁻ distribution pattern as well; however, overestimation especially in low latitudes may exist, especially in the tropical surface where [I⁻] ~~are~~is close to 500 nM among all the cGENIE-O₂ models (~~Fig. 4~~Fig. 5).

The cGENIE (internally generated oxygen distributions) vs WOA (imposed distributions) O₂ comparison provides evidence that I⁻ generated in low [O₂] settings may broadly enhance [I⁻] in oxygenated photic waters, with lower and closer-to-observations [I⁻] values in the WOA tunings (~~Fig. 4~~Fig. 5). This includes 'lifetime-threshold', where O₂ only impacts the reductive portion of the iodine cycle, but also the "'Fennel'" and "'reminO2lifetime'" where rates of I⁻ oxidation ~~is~~are also [O₂] dependent. More specifically, most of the elevated (~~over~~> 200 nM) surface [I⁻] in cGENIE, occurs in the ETSP and the northern Indian Ocean and corresponds to locations of high primary productivity (Fig. S6). Since the surface ocean [O₂] in the model is never below 200 µM, O₂-dependent IO₃⁻ reduction at the ocean surface is unlikely. Instead, *ex situ* transport from proximal regions of subsurface anoxia is the most probable source of elevated I⁻. Indeed, the most prominent regions of I⁻ enrichment in the model occur near the Peruvian coast and in the Arabian Sea, where ODZs lie below the surface (Fig. S6). More detailed data-model comparison among these two areas is limited because the observation data are few (e.g., Farrenkopf and Luther, 2002 and Rapp et al., 2020). In contrast, the meridional trend of I⁻ in the surface Atlantic Ocean, where ODZs are less

29

698 developed, exhibits better agreement with both the observation and the Wadley et al., (2020) model (Fig. S6). The
699 overestimation of tropical ocean surface [I⁻] by cGENIE is hence likely to be associated with deficiencies in the
700 simulation of ODZ oxygenation.

701 ~~Importantly~~That said, modeled overestimations ~~in~~ of surface ocean [I⁻] may be difficult to ~~confirm~~ verify
702 given current observational data densities. ~~Specifically, a~~In comparing ~~comparison of~~ observational data to model-
703 latitudinal trends which have been masked to only include model grid points with corresponding observations,
704 ~~although~~ ~~show~~ the same broad trend of increasing [I⁻] in the low latitudes exists, there ~~but~~ ~~with~~ are fewer ~~so~~
705 ~~called~~incidents of apparent model over-estimation ~~"overestimations"~~ (Fig. ~~S7~~S8). More observations in surface ocean
706 [I⁻] from low latitudes ~~is required~~ are needed to better assess the validity of elevated modelled surface ocean [I⁻] in
707 some regions.

4.2.2. Global and basin-specific iodine depth profiles

709 All the ~~models~~iodine cycle schemes ~~,~~ (both cGENIE-[O₂] and WOA-forced~~,~~) generate a decrease in [I⁻] and increase
710 in [IO₃⁻] from the euphotic zone down to the deep abyssal zone across ocean basins, matching the primary-production-
711 driven pattern (~~Fig. 5~~Fig. 6). As discussed in the previous section, this surface maxima of [I⁻] in the oxygenated water
712 column is the result of biologically mediated reduction or release during cell senescence of phytoplankton. Below the
713 photic zone, [I⁻] is close to zero and IO₃⁻ becomes the dominant species. The deep ocean is mostly oxygenated and has
714 longer water residence times (several millennia, Matsumoto, (2007)) compared to the I⁻ lifetime (<40 years, Tsunogai,
715 (1971)), thus facilitating I⁻ oxidation in the absence of IO₃⁻ reduction in ODZs.

716 We note that there are multiple general discrepancies between observations and ~~data~~model output as well as
717 differences between the results of WOA ~~and~~ vs. cGENIE-[O₂] parameter tuning. In general, all models reproduce the
718 global average better, relative to the basin-specific profiles. We suggest that the global averaged profiles are a better
719 test of the cGENIE simulations because of sampling biases associated with individual basins. For example, the
720 discrepancy between the model and ~~the~~ observation~~s~~ ~~is~~ are prominent in the Pacific (~~Fig. 5~~Fig. 6). The observed Pacific
721 subsurface [I⁻] peak mirrors the [IO₃⁻] minima that occurs at depths where ODZs are present. This ODZ feature in the
722 averaged Pacific observation profile is likely the result of sampling bias since most of the observations from the Pacific
723 ~~were~~ are from the ETNP (Rue et al., 1997; Moriyasu et al., 2020), and thus do not reflect~~ing~~ the overall iodine
724 distribution in the Pacific Ocean (Fig. ~~S8~~S9). ~~As for the meridional trends, sampling bias is again demonstrated in~~
725 ~~a~~This conclusion is supported by depth profiles masked to only include modeled grid points with corresponding
726 observation data. For example, there is a ~~, with~~ a clear mid-depth ODZ feature in the ~~modeled~~ masked model Pacific
727 depth profile~~s~~ ~~s~~ due to extensive ODZ studies in this region (Fig. ~~S8~~S9). ~~A similar example is from the Indian Ocean,~~
728 ~~which we do not show, since most iodine subsurface data come from the ODZ, not normal marine, localities.~~ All this
729 said, while the general features of iodine speciation with depth are generally similar, our data compilation indicates
730 the potential for some basin-specific variations which require further research to validate and mechanistically
731 understand.

4.2.3. Iodine distribution within ODZs

One of the major goals of calibrating the iodine cycle in cGENIE is to ~~be able to~~ simulate the iodine behavior associated with ancient low oxygen settings. To assess this potential, we analyzed model performance for the ETNP (Rue et al., 1997; Moriyasu et al., 2020) where observation~~al~~ data are abundant and the areal extent of the ODZ is sufficiently large to be reflected in the model grid (Fig. 6)~~. Importantly, it should still be noted that cGENIE is best applied to understanding broad scale processes and thus the scope of the ETNP ODZ transect comparison is likely too fine resolution to expect a good match. That said, the~~The simulated reduction in IO_3^- to I^- generally overlaps with the extent of the ODZ (Fig. 6), which provides support for the use of cGENIE to understand the broad distribution of ancient $[IO_3^-]$ and $[O_2]$. ~~Other n~~Non-threshold model parameterization-combinations (not discussed here but shown in Fig. S4) did not replicate the ODZ feature in iodine speciation.

~~Across~~ In all model configurations assuming cGENIE-$[O_2]$, the most prominent discrepancy is an underestimation of the spatial extent and intensity of the IO_3^- depletion zone in the ETNP (Fig. 6) ~~because~~ — a consequence of simulated subsurface O_2 deficient area ~~is~~ being notably narrower than ~~that compared to~~ WOA climatology (Fig. 6, Fig. S5). ~~There~~ This is principally a consequence of relatively weak continental margin upwelling and Equatorial divergence, itself a consequence of the low resolution (both horizontally and vertically) model grid that the 3D ocean circulation component is implemented on together with its simplified physics (Marsh et al., 2011) ~~[Marsh et al., 2011]~~. Another consequence of the low resolution nature of the cGENIE model grid is that the extent of the ETNP is of the order of the size of an individual grid box and ~~are multiple factors that might affect the performance of simulating the O_2 cycle in cGENIE. The model might underestimate the intensity of gyres in the North and Tropical Pacific, resulting in the narrowed ODZs in these areas. Also, the pattern of upwelled nutrients into the surficial Tropical Pacific needs to be tuned to better replicate the productivity and the O_2 consumption during remineralization. Another source of uncertainty is that the short-term processes, such as seasonal or El Niño driven ODZ variations at the time of sample collection are not replicated in the cGENIE simulations. In addition, due to the low special resolution of cGENIE, the whole~~entire ETNP only covers the longitude range of three grids in the model framework (Figure~~.~~ 1). Meanwhile, the depth resolution is ~~close to~~ca. 100-200 m per layer ~~in the surface~~upper ocean~~,~~ which also limits the finer simulation of ODZ features. Awareness of these ~~uncertainties~~limitations highlights the importance of ~~the use~~focusing use of the model ~~to understand~~ on regional and global oxygenation features ~~— as supported by proxy constraints — and their mechanistic framework during paleoceanographic reconstructions,~~ as opposed to overinterpreting ~~unconstrained high-resolution or~~ local features. ~~We are indeed aware of these uncertainties associated with O2 simulation in cGENIE. However, as a model targeted to assist paleoredox reconstructions, broadly reconstructing ODZ features in a coarse spatial resolution is acceptable.~~

Other data-model misfits ~~might have arisen as a result of~~may be due to ~~additional~~ IO_3^--reduction dependencies not explicitly accounted for in the model. As discussed above, shipboard incubation and radiogenic-tracer-spiked rate calculation suggest that IO_3^- reduction is slow in the offshore ETNP ODZ (Hardisty et al., 2021). This could explain why measurable IO_3^- is present in the core of the ETNP ODZ (Fig. 6). This is further exacerbated in the Eastern Tropical South Pacific ODZ, where $[IO_3^-]$ remains above 250 nM in some studies (Cutter et al., 2018) but near detection limits in in others (Rapp et al., 2020), suggesting extreme spatiotemporal variability related to currently unconstrained factors. Further, while the capability of microbes using IO_3^- as an electron acceptor for

770 oxidizing organic matter has been confirmed in laboratory culture experiments (Councell et al., 1997; Reyes-Umana
771 et al., 2021; Yamazaki et al., 2020; Amachi et al., 2007; Farrenkopf et al., 1997), no study to date has demonstrated
772 non-O_2 dependent controls driving variable IO_3^- reduction rates.

773 An important factor contributing to elevated [I^-] in ODZs is benthic fluxes and reduction occurring within
774 the uppermost layers of marine sediments (akin to denitrification). To help account for this in our ~~M score~~M-score
775 and model calibration (see: methods section), 'excess' iodine (>500 nM total iodine) was filtered from our
776 observational dataset. The excess iodine originated from the sediment flux has been observed in ODZ water columns
777 contacting anoxic sediments (Chapman, 1983; Farrenkopf and Luther, 2002; Cutter et al., 2018; Moriyasu et al., 2020;
778 Scholz et al., 2024). We note that excess iodine ~~is~~ occurs explicitly as I^-, reflecting the limited or lack of oxygen within
779 the ODZ, and is a local-regional phenomenon not yet observed to persist beyond ODZ settings. Future work can focus
780 on understanding the degree, if any, that excess I^- is oxidized to IO_3^-, and hence impacts the I/Ca paleoredox proxy.
781 ~~As such, since our goal is a paleoceanography focused model, cGENIE does not incorporate the benthic flux of I^-~~
782 ~~because only IO_3^- is tracked via the I:Ca~~I/Ca paleoredox proxy.

<aside>Formatted: Subscript</aside>

783

4.3. Applicability of the cGENIE marine iodine cycle to paleo redox reconstruction

785 ~~Parameter tuning, and the ability to reproduce modern observations, does not by itself offer any guarantee that spatial~~
786 ~~patterns are being simulated for the 'correct' reason (i.e., specific set and relative importance of mechanisms). This is~~
787 ~~even more pertinent in the context of the application of a modern-tuned model to paleo redox reconstruction. To test~~
788 ~~whether our new iodine cycle had predictive power in the geological past, we carried out a deep-time plausibility test.~~
789 ~~For the paleo plausibility test, we adopted the Cretaceous, pre-OAE2 (ca. 93 Ma) configuration (continental~~
790 ~~arrangement and ocean bathymetry, wind stress and velocity, and zonal average planetary albedo boundary conditions)~~
791 ~~from Monteiro et al., (2012). We choose this particular geological interval because the controls on ocean redox have~~
792 ~~been previously evaluated using the GENIE model (Monteiro et al., 2012; Hülse et al., 2019), the oceanic conditions~~
793 ~~are much more extensively dysoxic and anoxic than present-day and hence represent a relatively severe test of the~~
794 ~~model iodine cycle, and a number of I:Ca~~I/Ca proxy measurements are available (Zhou et al., 2015). In order to
795 ~~evaluate the same configuration of the iodine cycle as optimized in this study, we also substituted the temperature~~
796 ~~independent representation of biological export production and fixed remineralization profile of POM in the water~~
797 ~~column (i.e., Ridgwell et al., (2007)) for the temperature-dependent scheme of Crichton et al., (2021). However, in~~
798 ~~substituting the biological pump scheme in the model we change the ocean redox landscape compared with e.g.,~~
799 ~~Monteiro et al., (2012). We therefore test a range of different assumptions regarding the ocean PO_4 inventory at the~~
800 ~~time as a means of generating a range of different plausible states of ocean oxygenation. In this, we test: 0.2, 0.4, 0.6,~~
801 ~~0.8, 1.0, and 1.5 times the mean modern concentration (2.15 mM). We run the model with each of the best-fit (highest~~
802 ~~M score) sets of parameter values associated with the 5 different parameterization combinations (but focus on the~~
803 ~~results of the same 3 combinations we did for comparison against modern), and for each of the varying PO_4 inventory~~
804 ~~assumptions, for 10,000 years to steady-state.~~

805
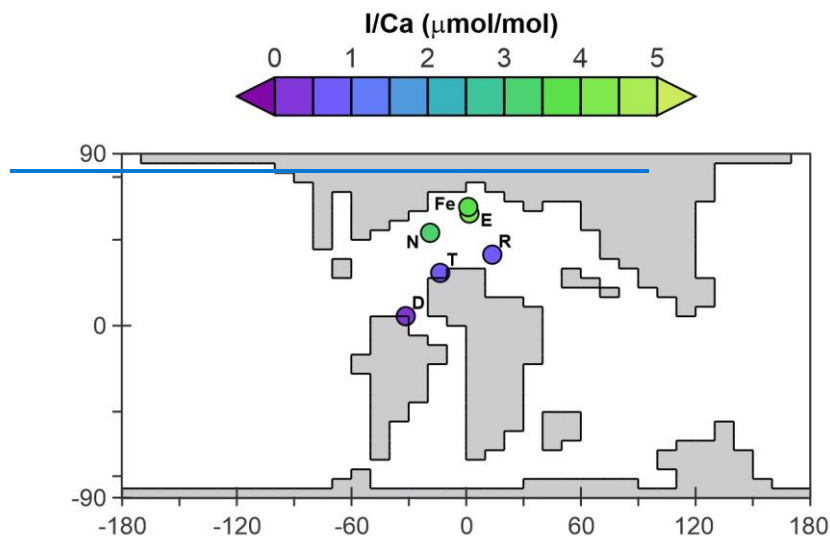
Figure 7: The continental setting during the Cretaceous OAE2 (Cenomanian - Turonian) in cGENIE. The colored dots represent averaged pre-OAE2 I:CaI/Ca measurements from each of the sections. D = Demerara Rise; E = Eastbourne; Fe = South Ferriby; N = Newfoundland; R = Raia del Pedale; T = Tarfaya.

The I:CaI/Ca data used for comparison with the model come from 6 sections (Zhou et al., 2015, Fig. 7, listed in Table S3). The pre-OAE2 I:CaI/Ca baseline value from each section is estimated through averaging the pre-CIE I:CaI/Ca measurements from Table S1 of Zhou et al., (2015). Diagenesis of carbonate hosted I/Ca tends to lower the primary values(Hardisty et al., 2017). However, such an offset is hard to quantitatively predict based on our current knowledge. In addition, according to Zhou et al., (2015), from which we adopted the I/Ca data, most of the sections only suffered minor diagenesis. To simplify the Cretaceous I/Ca IO_3^- conversion, we regard the measured I/Ca as primary and acknowledge there is potential uncertainty. For quantitative comparison between the model and the I:CaI/Ca data, we create an empirically derived forward proxy model for I:CaI/Ca. In this, we took the simulated concentration of IO_3^- and Ca^{2+} in the ocean surface layer of the model at every ocean grid point, and applied the temperature-dependent linear incorporation relationship derived from inorganic calcite synthesis experiment of Zhou et al., (2014), to estimate I:CaI/Ca. Specifically, the distribution coefficient (K_D) between I/Ca and [IO_3^-] ($K_D = (I/Ca)/[IO_3^-]$) shows linear dependency with temperature (Fig. S3 in Zhou et al., 2014). For our Cretaceous model calibration, we interpolated the K_Ds based on local temperature (at each grid associated with sections) simulated by cGENIE. I/CaThe converted modelled I:CaI/Ca at each section were then directly compared with the mean pre-OAE2 I:CaI/Ca measurements using the M scoreM-score (Fig. 8). We then extracted simulated I:CaI/Ca values from the model grid points corresponding to the sections reported by Zhou et al., (2015) and calculated the M-score. The statistical results

33

827 of this comparison are illustrated in Fig. 8 for the 3 parameterizations chosen for focus in the main text and for Fig.
828 S9 S10 for the full parameterization combinations and for parameter calibrations derived from internally and WOA
829 forced dissolved oxygen distributions. Beyond temperature, we acknowledge that IO_3^- incorporation into carbonate
830 lattice through substitution $IO_3^- + Na^+ \leftrightarrow CO_3^{2-} + Ca^{2+}$ is controlled by $[Na^+]$, $[CO_3^{2-}]$, and $[Ca^{2+}]$ (Podder et al., 2017).
831 However, either quantifying these ions during the Cretaceous seawater or quantitative calculation of ion substitution
832 dynamics requires further constraints. Although uncertainties are inevitable, we assume our temperature controlled
833 $[IO_3^-]$ I/Ca conversion based on current quantitative knowledge meets the requirement for Cretaceous model-data
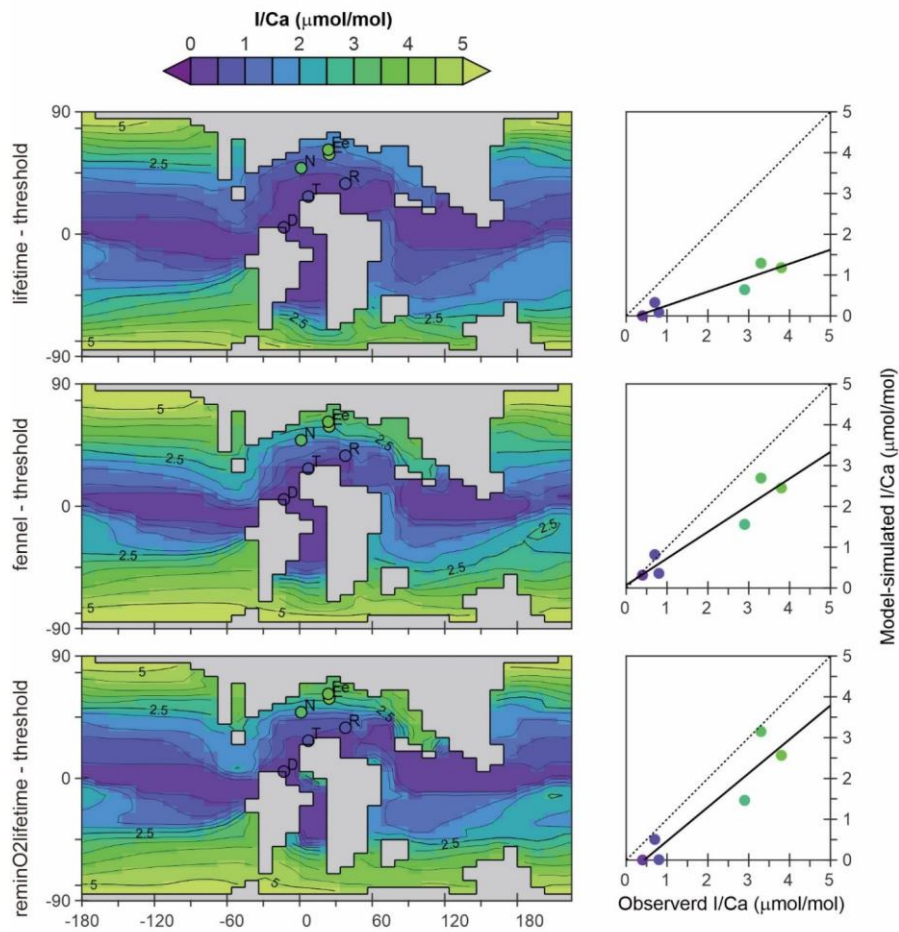834 comparison.

835
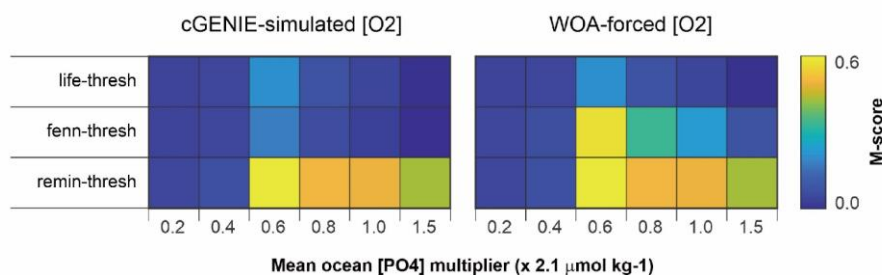
836

837 **Figure 8. The model skill scores of modeled and measured I:Ca I/Ca during the pre-OAE2. The iodine cycling**
838 **parameters are derived from modern simulations with cGENIE-simulated [O₂] and WOA-forced [O₂],**
839 **respectively. lifetime-thresh = lifetime-threshold; remin-thresh +DOC = reminO2lifetime-threshold +DOC**
840 **remineralization; remin-thresh = reminO2lifetime-threshold; fenn-thresh = fennel-threshold; life-inhib =**
841 **lifetime-inhibition; remin-thresh = reminO2lifetime-threshold life-remin +DOC = lifetime-reminSO4lifetime**
842 **+DOC remineralization; life-remin = lifetime-reminSO4lifetime.**

843

844   Most of the parameterization combinations tested reach their highest M score M-scores under the assumption
845 of 0.6-0.8 × modern [PO₄] (Fig. S9 S10). Previous analysis using the same climatological configuration of the GENIE
846 model indicated a PO₄ inventory of 1.0 x modern was most consistent with geological redox-related observations prior
847 to OAE2 (Monteiro et al., 2012). However, our assumption here of temperature-dependent POM export and
848 remineralization leads to higher export and shallower more intense ODZs compared to temperature-invariant
849 biological scheme (see: Crichton et al., (2021)). Hence, for a similar degree of ocean anoxia, we would expect the
850 need for a slightly lower nutrient inventory, as we indeed find.
851   In terms of the I:Ca I/Ca M-score, we find the parameterization combinations "reminO2lifetime-
852 threshold" 'reminO2lifetime threshold' and "fennel-threshold" 'fennel threshold' better replicate the geological
853 observations compared to the "lifetime threshold" 'lifetime threshold'. In general, WOA-derived parameter sets
854 perform better than those derived from cGENIE [O₂], again hinting at the importance of reducing the uncertainties in
855 simulating the modern O₂ cycle in cGENIE. These observations are also largely independent of the ocean PO₄
856 inventory assumption. Although we tested additional parameters in this study (Table S1), only those combinations

857 listed in Table 1 ("lifetime - threshold", "lifetime reminO2lifetime", "lifetime - Fennel") perform well in replicating

858 iodine gradients within the modern ocean (Figs. S2-4).Although combinations of parameterizations such as

859 "reminO2lifetime threshold"'reminO2lifetime threshold' with DOC remineralization, "lifetime inhibition", and

860 "lifetime reminSO4lifetime", also produce elevated M scoreM-scores, these combinations do not perform well in

861 replicating iodine gradients within the modern ocean (Figs. S2-4). Thus, until there is a better mechanistic

862 understanding of IO₃⁻ reduction in the modern ocean, the safest choice is arguably to apply the parameterization that

863 best reproduces modern observations and hence retain use of the "threshold"'threshold' IO₃⁻ reduction

864 parameterization for paleo applications.

865   The pre-OAE2 comparison is revealing because it the observations encapsulates a strong gradient between

866 high and very low I:CaI/Ca (Fig. 7Fig. 3), reflecting respectively, high and low surface ocean concentrations of IO₃⁻

867 in the model. All three of the parameterization-combinations we focus on here (just focusing on with WOA-derived

868 parameter values) correctly lead to veryare capable of reproducing low I:CaI/Ca values in the lower latitudinal sections

869 (Demerara Rise, Tarfaya, and Raia del Pedale; Fig. 9), although with a tendency to slightly overestimate seawater

870 IO₃⁻ depletion (cross-plots in Fig. 9). Low ocean surface [IO₃⁻] is duoccurs in the model as a result ofe to the existence

871 of a circum-Equatorial band of intense sub-surface anoxia and short transport time to the surface (and hence limited

872 oxidation). In the higher latitudinal sections, including Newfoundland, Eastbourne, and South Ferriby, I:CaI/Ca values

873 tend to be underestimated to varying degrees (Fig. 9). It is possible that the total iodine inventory has varied through

874 Earth history relative to the modern-day value (~500 nM), which was adopted for our Cretaceous model. Indeed, the

875 overall underestimated I/Ca by cGENIE might be the result of overall higher Cretaceous total iodine inventory (Zhou

876 et al., 2015; Lu et al., 2018). However, such difference is easily masked by local-regional redox variation and is thus

877 difficult to track (Zhou et al., 2015). Due to the lack of evidence otherwise, we assume the average total iodine during

878 the Cretaceous is close to the modern, and the consistent I/Ca underestimation is caused by uncertainty in model

879 simulation. Compared However, compared to the 'lifetime'" parameterization, both 'reminO2lifetime'" and 'Ffennel'"

880 oxidation simulate the I:CaI/Ca values in these high latitudinal sections rather better, with the regression closer to the

881 1:1 line (dotted in Fig. 9). We find this relationship instructional for understanding controls in the modern iodine cycle,

882 which we discuss in more detail below.

Figure 9. The pre-OAE2 ~~I:Ca~~I/Ca field derived from cGENIE [IO₃⁻] simulations, and the comparison between modeled and observed ~~I:Ca~~I/Ca from sections.

We first note that both 'lifetime' and 'fennel' iodine oxidation parameterizations in conjunction with a threshold of iodate reduction and internally generated GENIE-[O_2], give rise to identical parameter values (Table 2). We infer that this is because the modern ocean is predominately well-oxygenated and hence there is little inhibition of I⁻ oxidation in practice. In the Cretaceous environment, although I⁻ oxidation inhibition should be widespread, the M-scores are similar (Fig. 8). The rate of I⁻ oxidation in well oxygenated seawater is likely then critical in explaining elevated ~~I:Ca~~I/Ca values at higher Cretaceous latitudes. However, simply decreasing the lifetime in the modern ocean

893 would result in an under estimation of surface ocean [I⁻]. The 'fennel-threshold' combination under WOA-[O₂] reveals

894 a trade-off that solves this— ~~–~~ a decreased I⁻ lifetime compensated for by increased rates of I⁻ release to the ocean

895 interior directly through the biological pump and elevated cellular I:C (3.5×10^{-4} mol/mol vs. 1.5×10^{-4} mol/mol). In the

896 Cretaceous ocean this combination allows for both sharper latitudinal gradients in [IO₃⁻] (and hence ~~I:Ca~~I/Ca) to

897 develop, as well as steeper vertical gradients which allow for non-zero ~~I:Ca~~I/Ca values at low latitudes to be captured

898 (cross-plot in Fig. 9). This slight enhancement of the upper ocean [IO₃⁻] gradient is also apparent in the present-day

899 analysis (~~Fig. 5~~Fig. 6). The combination of 'reminO2lifetime' with a reduction threshold works similarly ~~–~~—a shorter

900 lifetime for I⁻ under oxic conditions offset in the modern ocean by elevated cellular I:C (Table 2). However, in this

901 case, our gridded parameter search identifies the trade-off as producing the highest M-score for both modelled and

902 WOA oxygen distributions.

903   What we learn from this is that the cGENIE iodine cycle tuned to modern observations has predictive power

904 under a very different state of ocean oxygenation (and circulation and operation of biological pump). However, this

905 is not true for every choice of parameterization, and the simple 'lifetime-threshold' combination, which when

906 calibrated was statistically almost the best representation of the iodine cycle, was unable to reproduce the latitudinal

907 ~~I:Ca~~I/Ca gradients in the Cretaceous ocean. Shortening the lifetime (and adding an inhibition term) together with

908 increasing the assumed cellular I:C, ~~could~~ maintains fidelity in simulating the modern ocean ~~fidelity~~ whilst much

909 better capturing Cretaceous ~~I:Ca~~I/Ca. That even better representations of Cretaceous ~~I:Ca~~I/Ca were possible but at the

910 expense of reproducing modern observations adequately hints that improvements in our mechanistic understanding

911 are needed, although all of the above assumes that the simulation of the Cretaceous redox landscape is plausible.

912   One caveat to our paleo comparison is that ~~beca~~use the residence time of iodine in the ocean is only around

913 300 kyr, the dissolved iodine inventory of the Cretaceous ocean could have deviated substantially from the modern

914 seawater value that we assume here (500 nM). ~~It is possible that the total iodine inventory has varied through Earth~~

915 ~~history relative to the modern day value (~500 nM),.~~ ~~Indeed, the~~One possible explanation for the overall

916 underestimation ~~of~~ed I/Ca by cGENIE might then be~~ the result of overall higher~~ that the Cretaceous ~~total~~ iodine

917 inventory was higher than modern (Zhou et al., 2015; Lu et al., 2018). Even a moderate increase (ca. 20-40%) in the

918 ocean iodine inventory (which we did not test here) would presumably act to increase the slope of the regression lines

919 for the parameterization-combinations 'fennel-threshold' and 'reminO2lifetime-threshold' and bring them close to

920 the 1:1 line (Fig~~ure~~. 9). ~~However, such difference is easily masked by local-regional redox variation and is unlikely a~~

921 ~~primary control on IO₃⁻ availability in reducing oceans (Zhou et al., 2015). Due to the lack of evidence otherwise, we~~

922 ~~assume the average total iodine during the Cretaceous is close to the modern, and the consistent I:Ca~~I/Ca

923 ~~underestimation is caused by uncertainty in model simulation.~~ Another uncertainty concerns the potential impact on

924 carbonate I/Ca ratios of different-from-modern dissolved calcium concentrations in the Cretaceous ocean. The calcite

925 crystal growth experiments of Zhou et al. [2014] on which we base our model-simulated I/Ca values were carried out

926 in synthetic solutions and not seawater. The partition coefficient K_D was calculated as [I/Ca]/[IO₃⁻] and as a result our

927 model formulation is independent of the ambient Ca^{2+} concentration. New I/Ca carbonate precipitation experiments

928 that explicitly account for the geological range in seawater composition would help increase confidence in the model-

929 simulated I/Ca values and hence improve the model simulation comparison possible with geological observations.

4.4. Choice of marine iodine cycle representation in cGENIE

The risk in tuning model parameters to fit some data target is always that the processes being tuned are distorted to accommodate an underlying structural error with the model. In this paper we illustrated how sub-regional-scale ocean oxygenation features such as the Eastern Tropical North Pacific ODZ (Figure. 67) are poorly represented at the resolution of the cGENIE Earth system model, and how this can lead to deficiencies in the simulation of the marine iodine cycle in these regions. Indeed, we found an improved statistical fit to observed iodine speciation data when we imposed a dissolved oxygen climatology to the model the grid rather than use the internally -general model $[O_2]$ fields (Table 2). In the case of the 'Fennel' parameterization-combination, we end up with two different sets of parameter values – one associated with the best fit to iodine speciation data under cGENIE projected $[O_2]$, and one under WOA imposed $[O_2]$. Selecting this particular scheme for paleo applications would appear to create a conundrum – whether (a) to choose the cGENIE $[O_2]$ derived parameter value set, and accept that model deficiencies were being implicitly corrected for in simulating marine iodine cycling and hence imposing a potential bias on paleo I/Ca, or (b) accept WOA $[O_2]$ derived parameter values. The choice would arguably be to accept the less potentially biased parameter value set (b), particularly as the relatively small-scale ODZ features of the modern ocean may be expanded to the regional-to-global scale in deeper time oceans and hence the redox features driving iodate reduction would become much more tractable for a model of the resolution of cGENIE.

However, we note that this choice does not exist for parameterization-combinations 'lifetime-threshold' and 'reminO2lifetime-threshold'. In both cases the sets of optimal parameter values are the same, whether derived from cGENIE projected $[O_2]$ or WOA imposed $[O_2]$ (Table 2). This gives us confidence that both these schemes are relatively agnostic to the details of how the modern oxygen cycle is simulated, and that errors in the simulation of sub-regional-scale ocean oxygenation features are not critical. (We note that iodine speciation data is still fitted better under WOA imposed $[O_2]$.) The choice of how to best represent the marine iodine cycle in cGENIE is then a choice between 'lifetime-threshold', which has been used in a similar form previously (Lu et al., 2018) and is capable of the best fit to modern observations, or 'reminO2lifetime-threshold'. While 'lifetime-threshold' might be preferable for more recent geological time and ocean ODZs similar to the present-day, it fails to account for I/Ca contrasts under more extreme redox gradients (Figure. 9). Although more difficult to interpret mechanistically, in suppressing the rate of I^- oxidation under low ambient $[O_2]$, 'reminO2lifetime-threshold' appears to be the more appropriate paleo choice.

We note that to achieve improved simulation of sub-regional-scale features of the ocean redox landscape, future paleo cGENIE model I/Ca applications could make use of the coupled GENIE-PLASIM climate configuration (Holden et al., 2016) (Holden et al., 2016). In this, the ocean circulation model is implemented on a higher resolution grid (64×32 with 32 vertical levels) and includes a coupled atmospheric GCM component (hence enabling interannual variability). It is also capable of being configured with different continental configurations for paleo climate questions (e.g. Keery et al., 2018).

5. Conclusions

Using the cGENIE Earth system model, we performed a series of ensemble experiments to determine ~~parameter searches for~~ suitable parameterizations to represent the marine iodine cycle and identified the best performing combinations of parameter values ~~combinations~~ in each case. We found that the optimized parameter valuess associated with ~~IO_3^- planktonic uptake~~, water column IO_3^- reduction and I^- oxidation, plus IO_3^- planktonic uptake (and subsequence I^- release during remineralization), ~~are~~ all fell within the range of field and experiment observations and hence could be considered plausible. Three iodine cycling parameterization ~~-~~combinations, 'lifetime-threshold', 'reminO2lifetime-threshold', and 'fennel-threshold' ~~emerged~~ were considered as viable candidates following our tests of the global ocean model ~~M score~~M-score, and model-data comparisons made across specific iodine gradients (euphotic latitudinal distribution, depth distribution, and ODZ distribution). We further evaluated the plausibility of our parameterizations and their paleo and ocean deoxygenation applicability by contrasting forward-proxy model generated ~~I:Ca~~I/Ca values against observations, taking the (pre-OAE2) Cretaceous redox landscape as a case study. ~~While some model-data discrepancies emerge for both modern and paleo, these highlight that future observational and/or experimental work is necessary to better constrain modern iodine cycling mechanisms and related spatiotemporal heterogeneities.~~ While we ~~further identified~~ highlighted the importance of improving the simulation of dissolved oxygen distributions in models, ~~equally,~~ we also found that our conclusions regarding preferred parameterizations and even specific parameter values~~,~~ was not overly dependent on the specific details of the simulated modern OMZs. Overall, ~~our analysis gives us a degree of confidence that carbonate I:Ca~~I/Ca ~~ratios can be interpreted in terms of past ocean oxygenation using models such as 'cGENIE'. While~~while some model-data discrepancies emerge for both modern and paleo, these highlight that future observational and/or experimental work is necessary to better constrain modern iodine cycling mechanisms and related spatiotemporal heterogeneities but that representations of the marine iodine cycle in an Earth system model based on modern observations and mechanistic knowledge appear transferrable to interpreting the geological record of the I/Ca oxygenation proxy.

Code availability. The code for the version of the 'muffin' release of the cGENIE Earth system model used in this paper, is tagged as v0.9.54, and is assigned a DOI: 10.5281/zenodo.13376310.
Configuration files for the specific experiments presented in the paper can be found in the directory: genie-userconfigs/PUBS/published/Cheng_et_al.Biogeosciences.2024. Details of the experiments, plus the command line needed to run each one, are given in the readme.txt file in that directory. All other configuration files and boundary conditions are provided as part of the code release.
A manual detailing code installation, basic model configuration, tutorials covering various aspects of model configuration, experimental design, and output, plus the processing of results, is assigned a DOI: 10.5281/zenodo.1407657. ~~The code for the version of the 'muffin' release of the cGENIE Earth system model used in this paper, is tagged as v0.9.13, and is assigned a DOI: 10.5281/zenodo.3999080.~~
~~Configuration files for the specific experiments presented in the paper can be found in the directory: genie-userconfigs/PUBS/chengetal.BG.2020. Details of the experiments, plus the command line needed to run each one, are given in the readme.txt file in that directory. All other configuration files and boundary conditions are provided as part of the code release.~~
~~A manual detailing code installation, basic model configuration, tutorials covering various aspects of model configuration, experimental design, and output, plus the processing of results, is assigned a DOI: 10.5281/zenodo.4305997.~~

References

40

Amachi, S., Kawaguchi, N., Muramatsu, Y., Tsuchiya, S., Watanabe, Y., Shinoyama, H., and Fujii, T.: Dissimilatory iodate reduction by marine Pseudomonas sp. strain SCT, Appl. Environ. Microbiol., 73, 5725–5730, https://doi.org/10.1128/AEM.00241-07, 2007.

Boscolo-Galazzo, F., Crichton, K. A., Ridgwell, A., Mawbey, E. M., Wade, B. S., and Pearson, P. N.: Temperature controls carbon cycling and biological evolution in the ocean twilight zone, Science (80-.)., 371, 1148–1152, https://doi.org/10.1126/science.abb6643, 2021.

Bowman, C. N., Lindskog, A., Kozik, N. P., Richbourg, C. G., Owens, J. D., and Young, S. A.: Integrated sedimentary, biotic, and paleoredox dynamics from multiple localities in southern Laurentia during the late Silurian (Ludfordian) extinction event, Palaeogeogr. Palaeoclimatol. Palaeoecol., 553, 109799, https://doi.org/10.1016/j.palaeo.2020.109799, 2020.

Broecker, W. S. and Peng, T. H.: Tracers in the Sea., https://doi.org/10.1016/0016-7037(83)90075-3, 1983.

Campos, M. L. A. M., Farrenkopf, A. M., Jickells, T. D., and Luther, G. W.: A comparison of dissolved iodine cycling at the Bermuda Atlantic Time-series station and Hawaii Ocean Time-series station, Deep. Res. Part II Top. Stud. Oceanogr., 43, 455–466, https://doi.org/10.1016/0967-0645(95)00100-x, 1996.

Chance, R., Weston, K., Baker, A. R., Hughes, C., Malin, G., Carpenter, L., Meredith, M. P., Clarke, A., Jickells, T. D., Mann, P., and Rossetti, H.: Seasonal and interannual variation of dissolved iodine speciation at a coastal Antarctic site, Mar. Chem., 118, 171–181, https://doi.org/10.1016/j.marchem.2009.11.009, 2010.

Chance, R., Baker, A. R., Carpenter, L., and Jickells, T. D.: The distribution of iodide at the sea surface, Environ. Sci. Process. Impacts, 16, 1841–1859, https://doi.org/10.1039/c4em00139g, 2014.

Chance, R., Tinel, L., Sherwen, T., Baker, A., Bell, T., Brindle, J., Campos, M., Croot, P., Ducklow, H., He, P., Hoogakker, B., Hopkins, F., Hughes, C., Jickells, T., Loades, D., Reyes Macaya, D., Mahajan, A., Malin, G., Phillips, D., Sinha, A., Sarkar, A., Roberts, I., Roy, R., Song, X., Winklebauer, H., Wuttig, K., Yang, M., Zhou, P., and Carpenter, L.: Global sea-surface iodide observations, 1967-2018., https://doi.org/doi:10.5285/7e77d6b9-83fb-41e0-e053-6c86abc069d0, 2019.

Chapman, P.: Changes in iodine speciation in the Benguela current upwelling system, Deep Sea Res. Part A, Oceanogr. Res. Pap., 30, 1247–1259, https://doi.org/10.1016/0198-0149(83)90083-3, 1983.

Councell, T. B., Landa, E. R., and Lovley, D. R.: Microbial reduction of iodate, Water. Air. Soil Pollut., 100, 99–106, 1997.

Crichton, K. A., Wilson, J. D., Ridgwell, A., and Pearson, P. N. P. N.: Calibration of temperature-dependent ocean microbial processes in the cGENIE.muffin (v0.9.13) Earth system model, Geosci. Model Dev., 14, 125–149, https://doi.org/10.5194/gmd-14-125-2021, 2021.

Cutter, G. A., Moffett, J. G., Nielsdóttir, M. C., and Sanial, V.: Multiple oxidation state trace elements in suboxic waters off Peru: In situ redox processes and advective/diffusive horizontal transport, Mar. Chem., 201, 77–89, https://doi.org/10.1016/j.marchem.2018.01.003, 2018.

Dalsgaard, T., Stewart, F. J., Thamdrup, B., De Brabandere, L., Revsbech, N. P., Ulloa, O., Canfield, D. E., and Delong, E. F.: Oxygen at nanomolar levels reversibly suppresses process rates and gene expression in anammox and denitrification in the oxygen minimum zone off Northern Chile, MBio, 5, 1–14,

1059   https://doi.org/10.1128/mBio.01966-14, 2014.

1060   Ding, Y., Sun, W., Liu, S., Xie, J., Tang, D., Zhou, X., Zhou, L., Li, Z., Song, J., Li, Z., Xu, H., Tang, P., Liu, K.,

1061   Li, W., and Chen, D.: Low oxygen levels with high redox heterogeneity in the late Ediacaran shallow ocean:

1062   Constraints from I/(Ca + Mg) and Ce/Ce* of the Dengying Formation, South China, Geobiology, 20, 790–809,

1063   https://doi.org/10.1111/gbi.12520, 2022.

1064   Edwards, A. and Truesdale, V. W.: Regeneration of inorganic iodine species in loch etive, a natural leaky incubator,

1065   Estuar. Coast. Shelf Sci., 45, 357–366, https://doi.org/10.1006/ecss.1996.0185, 1997.

1066   Edwards, C. T., Fike, D. A., Saltzman, M. R., Lu, W., and Lu, Z.: Evidence for local and global redox conditions at

1067   an Early Ordovician (Tremadocian) mass extinction, Earth Planet. Sci. Lett., 481, 125–135,

1068   https://doi.org/10.1016/j.epsl.2017.10.002, 2018.

1069   Edwards, N. R. and Marsh, R.: Uncertainties due to transport-parameter sensitivity in an efficient 3-D ocean-climate

1070   model, Clim. Dyn., 415–433, https://doi.org/10.1007/s00382-004-0508-8, 2005.

1071   Elderfield, H. and Truesdale, V. W.: On the biophilic nature of iodine in seawater, Earth Planet. Sci. Lett., 50, 105–

1072   114, https://doi.org/10.1016/0012-821X(80)90122-3, 1980.

1073   Fang, H., Tang, D., Shi, X., Zhou, L., Zhou, X., Wu, M., Song, H., and Riding, R.: Early Mesoproterozoic Ca-

1074   carbonate precipitates record fluctuations in shallow marine oxygenation, Precambrian Res., 373, 106630,

1075   https://doi.org/10.1016/j.precamres.2022.106630, 2022.

1076   Farrenkopf, A. M. and Luther, G. W.: Iodine chemistry reflects productivity and denitrification in the Arabian Sea:

1077   Evidence for flux of dissolved species from sediments of western India into the OMZ, Deep. Res. Part II Top. Stud.

1078   Oceanogr., 49, 2303–2318, https://doi.org/10.1016/S0967-0645(02)00038-3, 2002.

1079   Farrenkopf, A. M., Dollhopf, M. E., Chadhain, S. N., Luther, G. W., and Nealson, K. H.: Reduction of iodate in

1080   seawater during Arabian Sea shipboard incubations and in laboratory cultures of the marine bacterium Shewanella

1081   putrefaciens strain MR-4, Mar. Chem., 57, 347–354, https://doi.org/10.1016/S0304-4203(97)00039-X, 1997.

1082   Fennel, K., Follows, M., and Falkowski, P. G.: The co-evolution of the nitrogen, carbon and oxygen cycles in the

1083   Proterozoic ocean, Am. J. Sci., 305, 526–545, 2005.

1084   Garcia, H. E., Weathers, K., Paver, C. R., Smolyar, I., Boyer, T. P., Locarnini, R. A., Zweng, M. M., Mishonov, A.

1085   V., Baranova, O. K., Seidov, D., and Reagan, J. R.: Volume 3: Dissolved Oxygen, Apparent Oxygen Utilization, and

1086   Oxygen Saturation. A. Mishonov Technical Ed.; NOAA Atlas NESDIS 83, World Ocean Atlas 2018, 38 pp., 2018.

1087   Hardisty, D. S., Lu, Z., Planavsky, N. J., Bekker, A., Philippot, P., Zhou, X., and Lyons, T. W.: An iodine record of

1088   Paleoproterozoic surface ocean oxygenation, Geology, 42, 619–622, https://doi.org/10.1130/G35439.1, 2014.

1089   Hardisty, D. S., Lu, Z., Bekker, A., Diamond, C. W., Gill, B. C., Jiang, G., Kah, L. C., Knoll, A. H., Loyd, S. J.,

1090   Osburn, M. R., Planavsky, N. J., Wang, C., Zhou, X., and Lyons, T. W.: Perspectives on Proterozoic surface ocean

1091   redox from iodine contents in ancient and recent carbonate, Earth Planet. Sci. Lett., 463, 159–170,

1092   https://doi.org/10.1016/j.epsl.2017.01.032, 2017.

1093   Hardisty, D. S., Horner, T. J., Wankel, S. D., Blusztajn, J., and Nielsen, S. G.: Experimental observations of marine

1094   iodide oxidation using a novel sparge-interface MC-ICP-MS technique, Chem. Geol., 532, 119360,

1095   https://doi.org/10.1016/j.chemgeo.2019.119360, 2020.

Hardisty, D. S., Horner, T. J., Evans, N., Moriyasu, R., Babbin, A. R., Wankel, S. D., Moffett, J. W., and Nielsen, S. G.: Limited iodate reduction in shipboard seawater incubations from the Eastern Tropical North Pacific oxygen deficient zone, Earth Planet. Sci. Lett., 554, 116676, https://doi.org/10.1016/j.epsl.2020.116676, 2021.

Hashim, M. S., Burke, J. E., Hardisty, D. S., and Kaczmarek, S. E.: Iodine incorporation into dolomite: Experimental constraints and implications for the iodine redox proxy and Proterozoic Ocean, Geochim. Cosmochim. Acta, 338, 365–381, https://doi.org/10.1016/j.gca.2022.10.027, 2022.

He, P., Hou, X., and Aldahan, A.: Iodine isotopes species fingerprinting environmental conditions in surface water along the northeastern Atlantic Ocean, Sci. Rep., 3, 1–9, https://doi.org/10.1038/srep02685, 2013.

Hepach, H., Hughes, C., Hogg, K., Collings, S., and Chance, R.: Senescence as the main driver of iodide release from a diverse range of marine phytoplankton, Biogeosciences, 17, 2453–2471, https://doi.org/10.5194/bg-17-2453-2020, 2020.

Holden, P. B., Edwards, N. R., Fraedrich, K., Kirk, E., Lunkeit, F., and Zhu, X.: PLASIM-GENIE v1.0: A new intermediate complexity AOGCM, Geosci. Model Dev., 9, 3347–3361, https://doi.org/10.5194/gmd-9-3347-2016, 2016.

Hughes, C., Barton, E., Hepach, H., Chance, R., Wadley, M. R., Pickering, M. D., Hogg, K., Pommerening-r, A., Stevens, D. P., and Jickells, T. D.: Oxidation of iodide to iodate by cultures of marine ammonia-oxidising bacteria, Mar. Chem., 234, https://doi.org/10.1016/j.marchem.2021.104000, 2021.

Hülse, D., Arndt, S., and Ridgwell, A.: Mitigation of Extreme Ocean Anoxic Event Conditions by Organic Matter Sulfurization, Paleoceanogr. Paleoclimatology, 34, 476–489, https://doi.org/10.1029/2018PA003470, 2019.

Jia-zhong, Z. and Whitfield, M.: KINETICS OF INORGANIC REDOX REACTIONS IN SEAWATER I . The reduction of iodate by bisulphide Micro-organisms play a dominant role in the diagenesis of organic-rich sediments . The oxidative breakdown of the organic matter , with the accom- panying reductio, Science (80-.)., 19, 121–137, 1986.

Jiang, Z., Cui, M., Qian, L., Jiang, Y., Shi, L., Dong, Y., Li, J., and Wang, Y.: Abiotic and Biotic Reduction of Iodate Driven by Shewanella oneidensis MR-1 , Environ. Sci. Technol., https://doi.org/10.1021/acs.est.3c06490, 2023.

Keery, J. S., Holden, P. B., and Edwards, N. R.: Sensitivity of the Eocene climate to CO2 and orbital variability, Clim. Past, 14, 215–238, https://doi.org/10.5194/cp-14-215-2018, 2018.

Kerisit, S. N., Smith, F. N., Saslow, S. A., Hoover, M. E., Lawter, A. R., and Qafoku, N. P.: Incorporation Modes of Iodate in Calcite, Environ. Sci. Technol., 52, 5902–5910, https://doi.org/10.1021/acs.est.8b00339, 2018.

Laws, E. A., Falkowski, P. G., Smith, W. O., Ducklow, H., and James J McCarthy: Temperature effects on export production in the open ocean, Global Biogeochem. Cycles, 14, 1231–1246, 2000.

Liu, A., Tang, D., Shi, X., Zhou, X., Zhou, L., Shang, M., Li, Y., and Fang, H.: Mesoproterozoic oxygenated deep seawater recorded by early diagenetic carbonate concretions from the Member IV of the Xiamaling Formation, North China, Precambrian Res., 341, 105667, https://doi.org/10.1016/j.precamres.2020.105667, 2020.

Lu, W., Ridgwell, A., Thomas, E., Hardisty, D. S., Luo, G., Algeo, T. J., Saltzman, M. R., Gill, B. C., Shen, Y., Ling, H. F., Edwards, C. T., Whalen, M. T., Zhou, X., Gutchess, K. M., Jin, L., Rickaby, R. E. M., Jenkyns, H. C.,

43

Lyons, T. W., Lenton, T. M., Kump, L. R., and Lu, Z.: Late inception of a resiliently oxygenated upper ocean, Science (80-.)., 361, 174–177, https://doi.org/10.1126/science.aar5372, 2018.

Lu, W., Rickaby, R. E. M., Hoogakker, B. A. A., Rathburn, A. E., Burkett, A. M., Dickson, A. J., Martínez-Méndez, G., Hillenbrand, C. D., Zhou, X., Thomas, E., and Lu, Z.: I/Ca in epifaunal benthic foraminifera: A semi-quantitative proxy for bottom water oxygen in a multi-proxy compilation for glacial ocean deoxygenation, Earth Planet. Sci. Lett., 533, https://doi.org/10.1016/j.epsl.2019.116055, 2020a.

Lu, W., Dickson, A. J., Thomas, E., Rickaby, R. E. M., Chapman, P., and Lu, Z.: Refining the planktic foraminiferal I/Ca proxy: Results from the Southeast Atlantic Ocean, Geochim. Cosmochim. Acta, 287, 318–327, https://doi.org/10.1016/j.gca.2019.10.025, 2020b.

Lu, Z., Jenkyns, H. C., and Rickaby, R. E. M.: Iodine to calcium ratios in marine carbonate as a paleo-redox proxy during oceanic anoxic events, Geology, 38, 1107–1110, https://doi.org/10.1130/G31145.1, 2010.

Lu, Z., Hoogakker, B. A. A., Hillenbrand, C.-D., Zhou, X., Thomas, E., Gutchess, K. M., Lu, W., Jones, L., and Rickaby, R. E. M.: Oxygen depletion recorded in upper waters of the glacial Southern Ocean, Nat. Commun., 7, 1–8, https://doi.org/10.1038/ncomms11146, 2016.

Luther, G. W.: Review on the physical chemistry of iodine transformations in the oceans, Front. Mar. Sci., 10, 1–16, https://doi.org/10.3389/fmars.2023.1085618, 2023.

Luther, G. W. and Campbell, T.: Iodine speciation in the water column of the Black Sea, Deep Sea Res. Part A. Oceanogr. Res. Pap., 38, S875–S882, https://doi.org/10.1016/s0198-0149(10)80014-7, 1991.

Luther, G. W., Wu, J., and Cullen, J. B.: Redox Chemistry of Iodine in Seawater, Adv. Chem., 135–155, 1995.

Luther, W.: Iodine Chemistry in the Water the Chesapeake Bay : Evidence Iodine Forms Column of for Organic, Esruarine, Coast. Shelf Sci., 32, 267–279, 1991.

Marsh, R., Müller, S. A., Yool, A., and Edwards, N. R.: Incorporation of the C-GOLDSTEIN efficient climate model into the GENIE framework: "eb_go_gs" configurations of GENIE, Geosci. Model Dev., 4, 957–992, https://doi.org/10.5194/gmd-4-957-2011, 2011.

Martin, T. S., Primeau, F., and Casciotti, K. L.: Modeling oceanic nitrate and nitrite concentrations and isotopes using a 3-D inverse N cycle model, Biogeosciences, 347–367, 2019.

Matsumoto, K.: Radiocarbon-based circulation age of the world oceans, J. Geophys. Res. Ocean., 112, 1–7, https://doi.org/10.1029/2007JC004095, 2007.

Monteiro, F. M., Pancost, R. D., Ridgwell, A., and Donnadieu, Y.: Nutrients as the dominant control on the spread of anoxia and euxinia across the Cenomanian-Turonian oceanic anoxic event (OAE2): Model-data comparison, Paleoceanography, 27, https://doi.org/10.1029/2012PA002351, 2012.

Moriyasu, R., Evans, N., Bolster, K. M., Hardisty, D. S., and Moffett, J. W.: The Distribution and Redox Speciation of Iodine in the Eastern Tropical North Pacific Ocean, Global Biogeochem. Cycles, 34, 1–23, https://doi.org/10.1029/2019GB006302, 2020.

Moriyasu, R., Bolster, K. M., Hardisty, D. S., Kadko, D. C., Stephens, M. P., and Moffett, J. W.: Meridional survey of the Central Pacific reveals iodide accumulation in equatorial surface waters and benthic sources in the abyssal plain, Global Biogeochem. Cycles, https://doi.org/10.1029/2021GB007300, 2023.

1170 Panchuk, K., Ridgwell, A., and Kump, L. R.: Sedimentary response to Paleocene-Eocene thermal maximum carbon

1171 release: A model-data comparison, Geology, 36, 315–318, https://doi.org/10.1130/G24474A.1, 2008.

1172 Podder, J., Lin, J., Sun, W., Botis, S. M., Tse, J., Chen, N., Hu, Y., Li, D., Seaman, J., and Pan, Y.: Iodate in calcite

1173 and vaterite: Insights from synchrotron X-ray absorption spectroscopy and first-principles calculations, Geochim.

1174 Cosmochim. Acta, 198, 218–228, https://doi.org/10.1016/j.gca.2016.11.032, 2017.

1175 Pohl, A., Lu, Z., Lu, W., Stockey, R. G., Elrick, M., Li, M., Desrochers, A., Shen, Y., He, R., Finnegan, S., and

1176 Ridgwell, A.: Vertical decoupling in Late Ordovician anoxia due to reorganization of ocean circulation, Nat.

1177 Geosci., 14, 868–873, https://doi.org/10.1038/s41561-021-00843-9, 2021.

1178 Pohl, A., Ridgwell, A., Stockey, R. G., Thomazo, C., Keane, A., Vennin, E., and Scotese, C. R.: Continental

1179 configuration controls ocean oxygenation during the Phanerozoic, Nature, 608, 523–527,

1180 https://doi.org/10.1038/s41586-022-05018-z, 2022.

1181 Rapp, I., Schlosser, C., Barraqueta, J. M., Wenzel, B., Lüdke, J., and Scholten, J.: Controls on redox-sensitive trace

1182 metals in the Mauritanian oxygen minimum zone, 4157–4182, 2019.

1183 Rapp, I., Schlosser, C., Browning, T. J., Wolf, F., Le Moigne, F. A. C., Gledhill, M., and Achterberg, E. P.: El Niño-

1184 Driven Oxygenation Impacts Peruvian Shelf Iron Supply to the South Pacific Ocean, Geophys. Res. Lett., 47,

1185 https://doi.org/10.1029/2019GL086631, 2020.

1186 Reinhard, C. T. and Planavsky, N. J.: The History of Ocean Oxygenation, Ann. Rev. Mar. Sci., 14, 331–353,

1187 https://doi.org/10.1146/annurev-marine-031721-104005, 2022.

1188 Reinhard, C. T., Planavsky, N. J., Olson, S. L., Lyons, T. W., and Erwin, D. H.: Earth's oxygen cycle and the

1189 evolution of animal life, Proc. Natl. Acad. Sci. U. S. A., 113, 8933–8938, https://doi.org/10.1073/pnas.1521544113,

1190 2016.

1191 Reinhard, C. T., Olson, S. L., Turner, S. K., Pälike, C., Kanzaki, Y., and Ridgwell, A.: Oceanic and atmospheric

1192 methane cycling in the cGENIE Earth system model, Geosci. Model Dev., 1–45, https://doi.org/10.5194/gmd-2020-

1193 32, 2020.

1194 Remmelzwaal, S. R. C., Dixon, S., Parkinson, I. J., Schmidt, D. N., Monteiro, F. M., Sexton, P., Fehr, M. A.,

1195 Peacock, C., Donnadieu, Y., and James, R. H.: Investigating Ocean Deoxygenation During the PETM Through the

1196 Cr Isotopic Signature of Foraminifera, Paleoceanogr. Paleoclimatology, 34, 917–929,

1197 https://doi.org/10.1029/2018PA003372, 2019.

1198 Reyes-Umana, V., Henning, Z., Lee, K., Barnum, T. P., and Coates, J. D.: Genetic and phylogenetic analysis of

1199 dissimilatory iodate-reducing bacteria identifies potential niches across the world's oceans, ISME J.,

1200 https://doi.org/10.1038/s41396-021-01034-5, 2021.

1201 Ridgwell, A., Hargreaves, J. C., Edwards, N. R., Annan, J. D., Lenton, T. M., Marsh, R., Yool, A., and Watson, A.:

1202 Marine geochemical data assimilation in an efficient Earth system model of global biogeochemical cycling,

1203 Biogeosciences, 4, 87–104, https://doi.org/10.5194/bg-4-87-2007, 2007.

1204 Rue, E. L., Smith, G. J., Cutter, G. A., and Bruland, K. W.: The response of trace element redox couples to suboxic

1205 conditions in the water column, Deep. Res. Part I Oceanogr. Res. Pap., 44, 113–134, https://doi.org/10.1016/S0967-

1206 0637(96)00088-X, 1997.

1207 Schnur, A. A., Sutherland, K. M., Hansel, C. M., and Hardisty, D. S.: Rates and pathways of iodine speciation

1208 transformations at the Bermuda Atlantic Time Series, Front. Mar. Sci., 1–14,

1209 https://doi.org/10.3389/fmars.2023.1272870, 2024.

1210 Scholz, F., Hardisty, D. S., and Dale, A. W.: Early Diagenetic Controls on Sedimentary Iodine Release and Iodine-

1211 To-Organic Carbon Ratios in the Paleo-Record, Global Biogeochem. Cycles, 38,

1212 https://doi.org/10.1029/2023GB007919, 2024.

1213 Shang, M., Tang, D., Shi, X., Zhou, L., Zhou, X., Song, H., and Jiang, G.: A pulse of oxygen increase in the early

1214 Mesoproterozoic ocean at ca. 1.57–1.56 Ga, Earth Planet. Sci. Lett., 527, 115797,

1215 https://doi.org/10.1016/j.epsl.2019.115797, 2019.

1216 Ștreangă, I.-M., Repeta, D. J., Blusztajn, J. S., and Horner, T. J.: Speciation and cycling of iodine in the subtropical

1217 North Paci fi c Ocean, Front. Mar. Sci., 1–15, https://doi.org/10.3389/fmars.2023.1272968, 2024.

1218 Tang, D., Fang, H., Shi, X., Liang, L., Zhou, L., Xie, B., Huang, K., Zhou, X., Wu, M., and Riding, R.:

1219 Mesoproterozoic Molar Tooth Structure Related to Increased Marine Oxygenation, J. Geophys. Res.

1220 Biogeosciences, 128, 1–18, https://doi.org/10.1029/2022jg007077, 2023.

1221 Thamdrup, B., Dalsgaard, T., and Revsbech, N. P.: Widespread functional anoxia in the oxygen minimum zone of

1222 the Eastern South Pacific, Deep. Res. Part I Oceanogr. Res. Pap., 65, 36–45,

1223 https://doi.org/10.1016/j.dsr.2012.03.001, 2012.

1224 Truesdale, V. W., Bale, A. J., and Woodward, E. M. S.: The meridional distribution of dissolved iodine in near-

1225 surface waters of the Atlantic Ocean, Prog. Oceanogr., 45, 387–400, https://doi.org/10.1016/S0079-6611(00)00009-

1226 4, 2000.

1227 Truesdale, V. W., Watts, S. F., and Rendell, A. R.: On the possibility of iodide oxidation in the near-surface of the

1228 Black Sea and its implications to iodine in the general ocean, Deep. Res. Part I, 48, 2397–2412, 2001.

1229 Truesdale, V. W., Nausch, G., and Waite, T. J.: The effects of the 2001 Barotropic intrusion of bottom-water upon

1230 the vertical distribution of inorganic iodine in the Gotland Deep, Cont. Shelf Res., 55, 155–167,

1231 https://doi.org/10.1016/j.csr.2013.01.005, 2013.

1232 Tsunogai, S.: Iodine in the deep water of the ocean, Deep. Res., 18, 913–919, 1971.

1233 Uahengo, C. I., Shi, X., Jiang, G., and Vatuva, A.: Transient shallow-ocean oxidation associated with the late

1234 Ediacaran Nama skeletal fauna: Evidence from iodine contents of the Lower Nama Group, southern Namibia,

1235 Precambrian Res., 343, 105732, https://doi.org/10.1016/j.precamres.2020.105732, 2020.

1236 Wadley, M. R., Stevens, D. P., Jickells, T. D., Hughes, C., Chance, R., Hepach, H., Tinel, L., and Carpenter, L. J.: A

1237 Global Model for Iodine Speciation in the Upper Ocean, Global Biogeochem. Cycles, 34, 0–3,

1238 https://doi.org/10.1029/2019GB006467, 2020.

1239 Watterson, I. G.: Non-dimensional measures of climate model performance, Int. J. Climatol., 16, 379–391,

1240 https://doi.org/10.1002/(SICI)1097-0088(199604)16:4<379::AID-JOC18>3.0.CO;2-U, 1996.

1241 Wei, B., Tang, D., Shi, X., Lechte, M., Zhou, L., Zhou, X., and Song, H.: A Pulsed Oxygenation in Terminal

1242 Paleoproterozoic Ocean: Evidence From the Transition Between the Chuanlinggou and Tuanshanzi Formations,

1243 North China, Geochemistry, Geophys. Geosystems, 22, 1–23, https://doi.org/10.1029/2020GC009612, 2021.

1244 Wong, G. T. F. and Brewer, P. G.: The marine chemistry of iodine in anoxic basins, Geochim. Cosmochim. Acta,

1245 41, 151–159, https://doi.org/10.1016/0016-7037(77)90195-8, 1977.

1246 Wong, G. T. F., Takayanagi, K., and Todd, J. F.: Dissolved iodine in waters overlying and in the Orca Basin, Gulf of

1247 Mexico, Mar. Chem., 17, 177–183, https://doi.org/10.1016/0304-4203(85)90072-6, 1985.

1248 Wong, G. T. F., Piumsomboon, A. U., Dunstan, W. M., Wong, G. T. F., Piumsomboon, A. U., and Dunstan, W. M.:

1249 The transformation of iodate to iodide in marine phytoplankton cultures, Mar. Geol. Prog. Ser., 237, 27–39, 2002.

1250 Yamazaki, C., Kashiwa, S., Horiuchi, A., and Kasahara, Y.: A novel dimethylsulfoxide reductase family of

1251 molybdenum enzyme , Idr , is involved in iodate respiration by Pseudomonas sp . SCT, 22, 2196–2212,

1252 https://doi.org/10.1111/1462-2920.14988, 2020.

1253 Yu, Y., Chen, Y., Li, D., and Su, J.: A transient oxygen increase in the Mesoproterozoic ocean at ~1.44 Ga:

1254 Geochemical evidence from the Tieling Formation, North China Platform, Precambrian Res., 369, 106527,

1255 https://doi.org/10.1016/j.precamres.2021.106527, 2022.

1256 Zhang, S., Xu, C., Creeley, D., Ho, Y. F., Li, H. P., Grandbois, R., Schwehr, K. A., Kaplan, D. I., Yeager, C. M.,

1257 Wellman, D., and Santschi, P. H.: Response to comment on "iodine-129 and iodine-127 speciation in groundwater at

1258 hanford site, U.S.: Iodate incorporation into calcite," Environ. Sci. Technol., 47, 13205–13206,

1259 https://doi.org/10.1021/es4046132, 2013.

1260 Zhou, X., Thomas, E., Rickaby, R. E. M., Winguth, A. M. E., and Lu, Z.: I/Ca evidence for upper ocean

1261 deoxygenation during the PETM, Paleoceanography, 29, 964–975, https://doi.org/10.1002/2014PA002702, 2014.

1262 Zhou, X., Jenkyns, H. C., Owens, J. D., Junium, C. K., Zheng, X. Y., Sageman, B. B., Hardisty, D. S., Lyons, T. W.,

1263 Ridgwell, A., and Lu, Z.: Upper ocean oxygenation dynamics from I/Ca ratios during the Cenomanian-Turonian

1264 OAE 2, Paleoceanography, 30, 510–526, https://doi.org/10.1002/2014PA002741, 2015.

1265 Žic, V., Carić, M., and Ciglenečki, I.: The impact of natural water column mixing on iodine and nutrient speciation

1266 in a eutrophic anchialine pond (Rogoznica Lake, Croatia), Estuar. Coast. Shelf Sci., 133, 260–272,

1267 https://doi.org/10.1016/j.ecss.2013.09.008, 2013.

1268